Stellar Temporal Intensity Interferometry

Tan Peng Kian

A Thesis Submitted for the Degree of

Doctor of Philosophy

Department of Physics, National University of Singapore

Centre for Quantum Technologies

2015

進道若退
明道若昧

自强不息
飲水思源

Acknowledgements

This thesis is my personal gesamtkunstwerk over six years of doctoral candidature from 2010 to 2015. The aspiration is to implement novel, original astrophysical observations within the environmental, social and infrastructural realities of Singapore.

Such a journey is realised by coupling the experience and generosity in both time and effort of the experimental quantum optics group under the Centre for Quantum Technologies, with the astrophysics staff and the observatory support of the National University of Singapore.

It has been said that astronomy is a humbling experience, which is perhaps the defining character of this adventure. It is difficult, and assuredly inadequate to attempt to name and thank each person and memory individually and matter-of-factly, in this marriage of seeming polar opposites: quantum optics with astronomy, scientific research with public outreach, physics with the arts, home with everyone else.

Nothing I say nor do, can entirely paint how I feel for the bedrock that is family, the people who are the why of my life.

Taint a celestial vault for me in shades of blue,
and sprinkle stars over clear waters,
emulating musical notes floating through frozen times.
Give me a sandglass containing grains of memories,
take a photo of someone dancing through the prairie fields,
or maybe filter Paris's boulevards and cafes in vintage lens
– drown me in such ethereal worlds.

Thank you.

Declaration

I hereby declare that this thesis is my original work and it has been written by me in its entirety. I have duly acknowledged all the sources of information which have been used in the thesis.

This thesis has also not been submitted for any degree in any university previously.

Tan Peng Kian
11th April 2016

Abstract

Stellar intensity interferometry was developed by Hanbury-Brown & Twiss [1954, 1956b, 1957, 1958] to bypass the diffraction limit of telescope apertures, with successful measurements including the determination of 32 stellar angular diameters using the Narrabri Stellar Intensity Interferometer [Hanbury-Brown et al., 1974]. This was achieved by measuring the intensity correlations between starlight received by a pair of telescopes separated by varying baselines b which, by invoking the van Cittert-Zernicke theorem [van Cittert, 1934; Zernicke, 1938], are related to the angular intensity distributions of the stellar light sources through a Fourier transformation of the equal-time complex degree of coherence $\gamma(b)$ between the two telescopes. This intensity correlation, or the second order correlation function $g^{(2)}$ [Glauber, 1963], can be described in terms of two-photoevent coincidence measurements [Hanbury-Brown, 1974] for our use of photon-counting detectors.

The application of intensity interferometry in astrophysics has been largely restricted to the spatial domain but not found widespread adoption due to limitations by its signal-to-noise ratio [Davis et al., 1999; Foellmi, 2009; Jensen et al., 2010; LeBohec et al., 2008, 2010], although there is a growing movement to revive its use [Barbieri et al., 2009; Capraro et al., 2009; Dravins & Lagadec, 2014; Dravins et al., 2015; Dravins & LeBohec, 2007].

In this thesis, stellar intensity interferometry in the temporal domain is investigated instead. We present a narrowband spectral filtering scheme [Tan et al., 2014] that allows direct measurements of the Lorentzian temporal correlations, or photon bunching, from the Sun,

with the preliminary Solar $g^{(2)}(\tau = 0) = 1.3 \pm 0.1$, limited mostly by the photon detector response [Ghioni et al., 2008], compared to the theoretical value of $g^{(2)}(0) = 2$. The measured temporal photon bunching signature of the Sun exceeded the previous records of $g^{(2)}(0) = 1.03$ [Karmakar et al., 2012] and $g^{(2)}(0) = 1.04$ [Liu et al., 2014] by an order of magnitude.

In order to study possible effects of atmospheric turbulence [Blazej et al., 2008; Cavazzani et al., 2012; Dravins et al., 1997] on temporal intensity interferometry, the filtering scheme was improved so that the required integration time of measurement reduced from 45 minutes previously to only 4 minutes, which allowed for timing correlation measurements of Sunlight in 1° intervals of elevation angular position to probe the atmospheric dependence. The instruments were used to measure the temporal photon bunching signal of the Sun from 11:36 am to 5:36 pm, covering Solar elevation angles from approximately 70° just before noon to about 20° by the evening, corresponding to different depths of atmospheric air column [Bennett, 1982; Marini & Murray, 1973] the sunlight passed through. The thereby obtained Solar $g^{(2)}(\tau = 0) = 1.693 \pm 0.003$ exceeded our previous record, due to improved suppression of the blackbody spectrum outside the target bandwidth. The Solar photon bunching signature was compatible with control measurements of an Argon arc lamp with $g^{(2)}(\tau = 0) = 1.687 \pm 0.004$, which served as a blackbody light source of temperature $T = 6000\,\mathrm{K}$. This suggests that the atmospheric and weather conditions have no measurable effects on temporal intensity interferometry for a 2 GHz optical bandwidth after narrowband spectral filtering.

The instruments were exposed to a light source simulating astrophysical scenarios, created by mixing the blackbody radiation from the Argon arc lamp with laser light at 513.8 nm. The spectral filtering scheme was able to isolate the laser light by filtering the blackbody spectrum to only $\Delta\nu_{FWHM} \approx 2\,\mathrm{GHz}$ and thus suppressing the blackbody contribution to the order of 10^4 photoevents/sec. The instruments were thus able to identify coherent laser light contributions of 3×10^4 photoevents/sec within the blackbody spectrum, which is a situation that Optical SETI [Drake, 1961; Dyson, 1960; Forgan, 2014; Korpela et al., 2011; Merali, 2015; Sagan & Drake, 1975; Townes, 1983] may have to identify.

The final scenario tested was to identify the laser light at 513.8 nm that has been Doppler broadened by a suspension of mono-dispersive microspheres [Dravins & Lagadec, 2014; Dravins et al., 2015]. We found that $g^{(2)}(0) = 1.227 \pm 0.005$ and determined the coherence time of the broadened laser signal to be $\tau_c = 44 \pm 2\,\mathrm{ns}$, corresponding to a linewidth of about 23 MHz which is comparable to the predicted linewidth values for natural lasers [Dravins & Germanà, 2008; Griest et al., 2010; Johansson & Letokhov, 2005; Roche et al., 2012; Strelnitski et al., 1995; Taylor, 1983; Tellis & Marcy, 2015].

These results suggest that the narrowband spectral filtering technique developed in this thesis may provide a useful tool for revisiting intensity correlation measurements in astronomy again.

Contents

Nomenclature

Fundamental Physical Constants

π	3.14159
c	Speed of Light in Vacuum $= 2.99792 \times 10^{8}\,\mathrm{m{\cdot}s^{-1}}$
h	Planck Constant $= 6.62608 \times 10^{-34}\,\mathrm{J{\cdot}s}$
k_B	Boltzmann Constant $= 1.38066 \times 10^{-23}\,\mathrm{J{\cdot}K^{-1}}$

Symbols

α	Elevation Angle
$\mathcal{F}_{\mathcal{R}}$	Reflectivity Finesse
ΔT	Measurement Duration
δ	Declination
$\varnothing$	Diameter
η	Detector Quantum Efficiency
γ	Complex Degree of Coherence
λ	Wavelength
ϕ	Latitude
$\rho(\nu)$	Density of States

σ	Standard Deviation
τ	Timing Separation
τ_c	Coherence Time
τ_j	Timing Jitter
θ_s	Stellar Angular Diameter
E	Electric Field Amplitude
$g^{(1)}$	First Order Correlation Function
$g^{(2)}$	Second Order Correlation Function
J_1	Bessel Function of the First Kind, First Order
N	Number of Photoevents
$S(\nu)$	Spectral Density
V	Interferometric Visibility

Acronyms

ADC	Analog-to-Digital Converter
AOI	Angle of Incidence
APC	Angled Physical Contact
APD	Avalanche Photon Detector
AR	Anti-Reflection Coating
BNC	Bayonet Neill-Concelman
BPF	Bandpass Filter
BS	Non-Polarising Beam Splitter
CW	Continuous Wave

CWL	Central Wavelength
EFL	Effective Focal Length
FS	Fused Silica
FSR	Free Spectral Range
FWHM	Full-Width at Half-Maximum
GMT	Greenwich Mean Time
GPS	Global Positioning System
GT	Glan-Taylor Polariser
HBT	Hanbury-Brown and Twiss
HST	Hubble Space Telescope
HWP	Half-Wave Plate, also $\lambda/2$
IAU	International Astronomical Union
IRF	Instrument Response Function
LED	Light Emitting Diode
N-BK7	Non-Leaded Borosilicate Crown Glass
NA	Numerical Aperture
NASA	National Aeronautics and Space Administration
NIM	Nuclear Instrumentation Module
NSII	Narrabri Stellar Intensity Interferometer
NV	Nitrogen-Vacancy
PBS	Polarising Beam Splitter
PID	Proportional-Integral-Derivative

PMT	Photomultiplier Tube
QWP	Quarter-Wave Plate, also $\lambda/4$
SCT	Schmidt-Cassegrain Telescope
SETI	The Search for Extraterrestrial Intelligence
SMF	Single Mode Optical Fibre
SNR	Single-to-Noise Ratio
SPDC	Spontaneous Parametric Down Conversion
SUSI	Sydney University Stellar Interferometer
TEM	Transverse Electromagnetic
TTL	Transistor-Transistor Logic
VLT	Very Large Telescope

List of Figures

List of Tables

Chapter 1

Introduction

1.1 Stellar Intensity Interferometry

Stellar intensity interferometry was developed by Hanbury-Brown & Twiss [1954, 1957, 1958] to circumvent the diffraction limit of the conventional telescope, with an angular resolution θ_s that is constrained by the aperture size b, as can be described by [Fox, 2006]

$$\theta_s = 1.22\,\frac{\lambda}{b}\,. \tag{1.1}$$

With reference to Tab. 1.1, the Large Binocular Telescope (LBT) is one of the largest single-aperture optical telescope structure on a single mechanical mount [Allen, 2000], with two 8.4 m main mirrors spanning 22.8 m edge-to-edge, and thus a corresponding angular resolution of 6.1 mas (milli-arcseconds), which can resolve only a few stars such as Betelgeuse with an angular diameter in the range of ≈ 45 mas. In order to increase the effective angular resolution, arrays of telescopes with larger baselines b separating the telescopes are used instead [Labeyrie et al., 2006], such as the Sydney University Stellar Interferometer (SUSI) [Davis et al., 1999]. SUSI follows the more conventional Michelson design unlike its predecessor, the Narrabri Stellar Intensity Interferometer (NSII), with baselines up to 188 m which successfully determined the angular diameters of 32 stars [Hanbury-Brown et al., 1974].

⋆Star / Observatory	θ_s **[mas]**	b **[m]**
⋆Sun	1800000	0.00008
Hubble Space Telescope (HST)	60	2.4
⋆Betelgeuse	45	3
Large Binocular Telescope (LBT)	6.1	22.8
⋆Sirius	6	23
Sydney University Stellar Interferometer (SUSI)	0.2	640

Table 1.1: A list of angular resolution or angular size paired with the corresponding baseline or aperture size given by Eqn. 1.1, for some stars and telescopes [Allen, 2000]. Note that $\lambda = 550\,\mathrm{nm}$ is used and that $1^\circ = 60\,\mathrm{arcminutes}\,(') = 3600\,\mathrm{arcseconds}\,('') = 3600000$ milli-arcseconds (mas).

Spatial Intensity Interferometry

The Narrabri Stellar Intensity Interferometer (NSII) operated by the technique of spatial intensity interferometry [Hanbury-Brown & Twiss, 1957, 1958], which allows spatial information of stars to be extracted from a set of intensity correlation measurements [Fox, 2006; Loudon, 2000; Mandel & Wolf, 1995] by following the propagation of the stellar source coherence function to the aperture plane of the ground-based observers performing the intensity correlation measurements.

First consider the normalised first order correlation function $g^{(1)}$ between the electric fields $E(\vec{r}, t)$ at two points $\vec{r}_1, \vec{r}_2$ as described by

$$g^{(1)}(\vec{r}_1, t_1; \vec{r}_2, t_2) = \frac{\langle E^*(\vec{r}_1, t_1) E(\vec{r}_2, t_2) \rangle}{\sqrt{[\langle |E(\vec{r}_1, t_1)|^2 \rangle \langle |E(\vec{r}_2, t_2)|^2 \rangle]}}\,, \tag{1.2}$$

where $\langle ... \rangle$ denotes a time-averaging over the statistical ensemble:

$$\langle E^*(t) E(t+\tau) \rangle = \frac{1}{T} \int_T E^*(t) E(t+\tau) dt\,. \tag{1.3}$$

Correspondingly, the auto-correlation function of the electric field at one particular position, or where $\vec{r}_1 = \vec{r}_2 = \vec{r}$, describes the temporal cross-correlation of the source signal with itself at varying points in time.

By setting the constraint $t_1 = t_2 = t$, we obtain the equal-time complex degree of coherence $\gamma(\vec{r}_1, \vec{r}_2, t)$ which describes the normalised spatial first order correlation function between two observer positions $\vec{r}_1, \vec{r}_2$ at the same time t:

$$\gamma(\vec{r}_1, \vec{r}_2, t) = \frac{\langle E^*(\vec{r}_1, t) E(\vec{r}_2, t)\rangle}{\sqrt{[\langle |E(\vec{r}_1, t)|^2\rangle \langle |E(\vec{r}_2, t)|^2\rangle]}} \,. \tag{1.4}$$

For a pair of telescopes observing a distant star which is, through the use of bandpass filters, effectively a quasi-monochromatic incoherent light source in the far-field regime, the van Cittert-Zernicke theorem can be invoked which states that the Fourier transform of the complex spatial (equal-time $\tau = |t_1 - t_2| = 0$) coherence function $\gamma(\vec{r}_1, \vec{r}_2, \tau = 0)$ is the angular intensity distribution $I(\vec{r})$ of the light source [Labeyrie et al., 2006; van Cittert, 1934; Zernicke, 1938].

To extract spatial information from the equal-time complex degree of coherence between the two telescopes $\gamma(\vec{r}_1, \vec{r}_2, 0)$, we measure the interferometric fringe visibility $V(\vec{r}_1, \vec{r}_2)$ observed between the telescope pair, where A_1, A_2 are proportional to the intensities of starlight collected by each telescope at $\vec{r}_1, \vec{r}_2$ respectively:

$$V(\vec{r}_1, \vec{r}_2) = \frac{2A_1A_2}{A_1^2 + A_2^2} \cdot |\gamma(\vec{r}_1, \vec{r}_2)| \,, \tag{1.5}$$

such that if the two telescopes received equal contributions $A_1 = A_2$ from the stellar light source, then the spatial visibility $V(\vec{r}_1, \vec{r}_2)$ between the telescopes reduces to the modulus of the equal-time complex degree of coherence $\gamma(\vec{r}_1, \vec{r}_2, 0)$:

$$V(\vec{r}_1, \vec{r}_2) = |\gamma(\vec{r}_1, \vec{r}_2)| \,. \tag{1.6}$$

Under ideal circumstances, a conventional Michelson interferometer such as the Sydney University Stellar Interferometer can directly retrieve this spatial visibility information by measuring the fringe contrast between the maximal and minimal interference fringe intensities, corresponding to I_{max} and I_{min}, respectively:

$$V = \frac{I_{max} - I_{min}}{I_{max} + I_{min}} \,. \tag{1.7}$$

It follows that the interferometric visibility V scales from $V = 0$ where there are no interference fringes for $I_{max} = I_{min}$, to an upper bound of $V = 1$ for $I_{min} = 0$.

In practical circumstances however, it is difficult to perform visibility measurements by Michelson interferometry in astronomy, due to the phase ϕ dependence required for Michelson interference. Consider a quasi-monochromatic electric field $E(t)$ with a central frequency ω_0 [Fox, 2006]:

$$E(t) = E_0 e^{-i\omega_0 t} e^{i\phi(t)} \,, \tag{1.8}$$

with a corresponding complex degree of coherence $\gamma(\tau)$:

$$\gamma(\tau) = e^{-i\omega_0 \tau} \langle e^{i[\phi(t+\tau)-\phi(t)]} \rangle \,. \tag{1.9}$$

The real component $e^{-i\omega_0 \tau}$ follows an oscillatory behaviour defined by the central frequency ω_0, which results in observable interference fringes for timing differences τ shorter than the characteristic coherence time τ_c, such that when $\tau > \tau_c$, phases become completely uncorrelated. The oscillation amplitude define the fringe contrast and thus the visibility V.

The dependence on a phase ϕ in the time-averaged term $\langle e^{i[\phi(t+\tau)-\phi(t)]} \rangle$ requires that the opto-mechanical instrumentation must be maintained within sub-wavelength precision, i.e. tens of nanometres for optical light. Similarly, the atmospheric turbulence can perturb the optical path-lengths [Blazej et al., 2008; Cavazzani et al., 2012; Labeyrie et al., 2006] by many orders of 2π between the telescopes to the star, causing the $\langle e^{i[\phi(t+\tau)-\phi(t)]} \rangle$ term to vanish and thus negligible interferometric visibility.

However for the special case of thermal light sources, intensity interferometry can conveniently extract the visibility information without the phase ϕ dependence, through the relationship [Glauber, 1963; Mandel & Wolf, 1995]:

$$g^{(2)} = 1 + V^2 \,, \tag{1.10}$$

such that $g^{(2)}(0) = 1$ for a random incoherent light source, upwards to $g^{(2)}(0) = 2$ for an ideal thermal light source like blackbody radiation. The phase independence of intensity interferometry thus relaxes the requirements on opto-mechanical stability of the instrumentation, as well as atmospheric conditions in principle. This makes intensity interferometry a suitable technique to develop for astronomical observations.

To use spatial intensity interferometry to extract spatial information about a star, such as its stellar angular diameter θ_s, consider an ideal circular stellar profile with angular diameter θ_s and homogenous intensity distribution as observed by two telescopes with a baseline separation of $b = |\vec{r}_1 - \vec{r}_2|$.

Invoking the van Cittert-Zernicke theorem, the Fourier transform of such a homogenous and circular stellar intensity profile would result in the following complex spatial coherence function [Labeyrie et al., 2006]

$$\gamma(b) = \frac{2J_1(\nu)}{\nu}\,, \tag{1.11}$$

where J_1 corresponds to the Bessel function of the first kind, first order, and defined by the characteristic spatial frequency ν given by

$$\nu = \frac{\pi\theta_s}{\bar{\lambda}}b\,, \tag{1.12}$$

where θ_s is the angular diameter of the stellar source, $\bar{\lambda}$ is the mean wavelength observed, and baseline b is the mutual spatial separation of the telescopes.

The Bessel function has its first zero value at $J_1(\nu = 3.83) = 0$, with the corresponding spatial frequency

$$\frac{\pi\theta_s}{\bar{\lambda}}b_0 = 3.83\,, \tag{1.13}$$

which can be re-expressed into

$$\theta_s = 1.22\frac{\bar{\lambda}}{b_0}\,. \tag{1.14}$$

This is the Rayleigh criterion [Rayleigh, 1879] for the diffraction limit seen earlier in Eqn. 1.1, for a circular aperture of size b_0 with the small-angle approximation such that $\sin(\theta_s) \approx \theta_s$ which is valid for the far-field regime of starlight.

Combining the expressions for Eqn. 1.6, Eqn. 1.10 and Eqn. 1.11, in the case of an ideal circular stellar profile with homogenous intensity, we obtain the relationship between the spatial second order correlation $g^{(2)}(b)$ with the spatial intensity distribution of the stellar light source:

$$g^{(2)}(b) = 1 + \left|\frac{2J_1(\nu)}{\nu}\right|^2. \tag{1.15}$$

An example of the expected $g^{(2)}(b)$ behaviour for Sirius is illustrated in Fig. 1.1, assuming an angular diameter of 5.9 milli-arcseconds (mas) observed at a mean wavelength $\bar{\lambda} = 400\,\mathrm{nm}$. Sirius can be directly resolved by a baseline separation or aperture diameter of around 17 m, or extrapolated by fitting from a set of $g^{(2)}(b)$ correlation measurements using telescope baselines b shorter than the stellar coherent length b_0, which is how Hanbury-Brown [1974] determined the 32 stellar angular diameters using the Narrabri Stellar Intensity Interferometer.

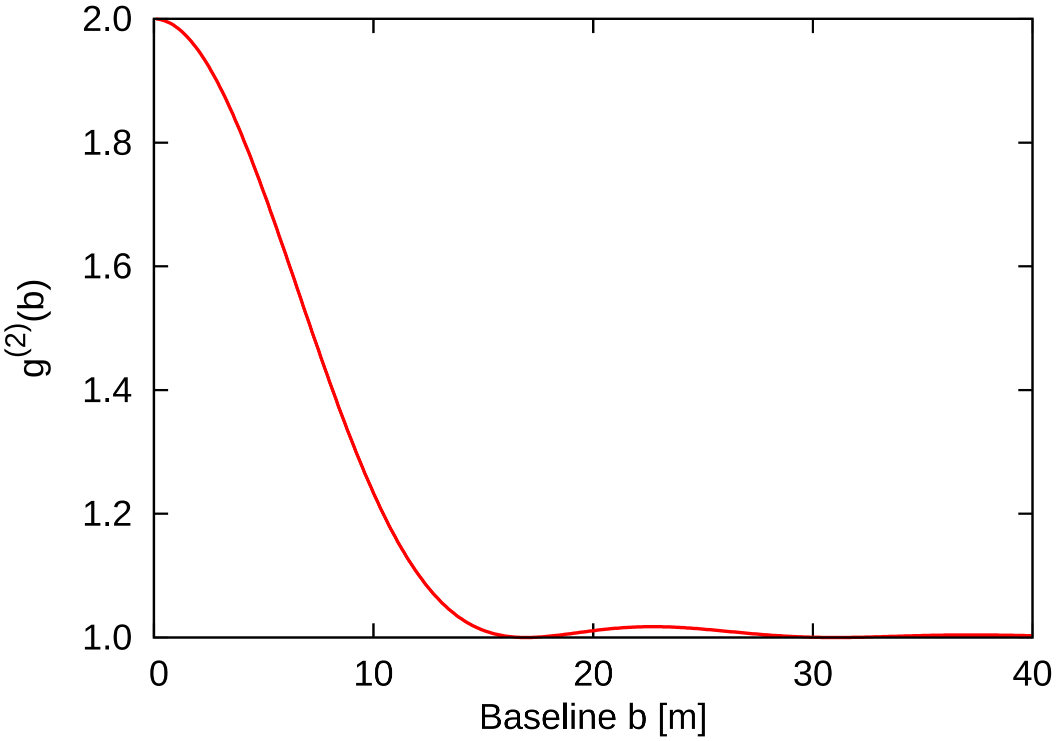

Figure 1.1: Ideal spatial $g^{(2)}(b)$ behaviour for Sirius at wavelength $\bar{\lambda} = 400\,\mathrm{nm}$, assuming a circular stellar profile with homogenous intensity distribution.

Two-Photon Coincidence Measurement

We translate the $g^{(2)}(b)$ expression in Eqn. 1.15 in terms of photoevent measurements to match our experimental scheme of using avalanche photon detectors (APDs) to measure and time-stamp photon timing arrivals at two detectors.

Consider a generalised second order correlation $g^{(2)}$ between two physical events denoted as 1 and 2, to be the joint probability $P_{1,2}$ of the coincidence event $N_{1,2}$ normalised by the probabilities P_1, P_2 of their individual events N_1, N_2:

$$g^{(2)} = \frac{P_{1,2}}{P_1 P_2}\,. \tag{1.16}$$

The probability P of an event can be evaluated as the product of the event rate r with the histogram bin width Δt:

$$P = r \cdot \Delta t\,, \tag{1.17}$$

where the rate r is empirically measured by the total number N of such events observed, averaged over the total measurement duration ΔT:

$$r = \frac{N}{\Delta T}\,. \tag{1.18}$$

These probability terms combines to give

$$\frac{P_{1,2}}{P_1 P_2} = \frac{\frac{N_{1,2}}{\Delta T}\Delta t}{\frac{N_1}{\Delta T}\Delta t \cdot \frac{N_2}{\Delta T}\Delta t}\,, \tag{1.19}$$

which can be simplified to the practical expression

$$g^{(2)} = \frac{N_{1,2}}{N_1 N_2}\frac{\Delta T}{\Delta t}\,. \tag{1.20}$$

Using photon-counting detectors, measurements for intensity interferometry are thus two-photon coincidence histograms, normalised by the single-event signal counts, scaling linearly proportional to the measurement duration and inversely to the histogram bin width. This expression suggests that in order to obtain higher statistical confidence in the measured $g^{(2)}$, we should try to maximise the measurement duration ΔT.

We optimise the histogram bin width by setting $\Delta t = \tau_j$, where τ_j is the detector timing jitter, which is the timing uncertainty of the photoevent measurement by the detector.

1.2 Limitations by the Signal-to-Noise Ratio

Despite the phase independence of stellar intensity interferometry allowing for large variable baselines and thus higher angular resolution, as well as robustness against the atmospheric and weather conditions, the technique has not found widespread adoption [Foellmi, 2009].

This is due to the limitations set in principle by its signal-to-noise ratio (SNR), which make further measurements impractical beyond the hottest stars already measured [Hanbury-Brown, 1974], and is also dependent on whether the photon detector timing resolution is able to resolve the characteristic coherence time τ_c of the stellar blackbody radiation source, where $\tau_c = 1/\Delta\nu$ for a well-defined spectral distribution with a full width at half maximum (FWHM) of $\Delta\nu$.

In the regime where the photon detector timing resolution is unable to resolve the coherent timescale of the stellar light source, which was the situation for Hanbury-Brown and Twiss (HBT), and when both telescopes are collecting similar intensities of starlight, the signal-to-noise ratio can be described in terms of the source coherence time τ_c, the rate r of photoevents received by each photon detector (APD), the spatial visibility $V(b)$ between the two telescopes separated by baseline b, the measurement duration ΔT and the histogram bin width Δt, by the expression [Hanbury-Brown, 1974]:

$$\mathrm{SNR} = \tau_c \frac{r}{2} V(b)^2 \sqrt{\frac{\Delta T}{2\Delta t}}\,. \tag{1.21}$$

The signal-to-noise ratio (SNR) increases under good atmospheric transparency conditions, due to a higher rate r of photoevents that can be collected by the telescopes. The photoevent rate r also implies that the SNR will increase by observing hotter stars with correspondingly higher spectral density $S(\nu)$, and by using photon detectors with higher quantum efficiency.

The use of larger telescope apertures would also increase the rate r of photoevents received by the detectors, but only if the aperture diameter remains shorter than the coherent length b_0, otherwise the spatial visibility term will reduce significantly once the telescope aperture exceeds the coherent length.

Longer measurement durations ΔT and lower photon detector timing jitters τ_j that allow for shorter histogram bin widths Δt will also raise the signal-to-noise ratio of the intensity interferometry measurement.

Although the SNR expression in Eqn. 1.21 contains a coherence time τ_c contribution, attempts to increase it by spectral filtering will result in a corresponding reduction in the rate r of photoevents received, such that the combined term $r\tau_c$ remains constant, and so make the signal-to-noise ratio independent of the optical bandpass and thus unaffected by spectral filtering in principle.

When the photon detector timing jitter τ_j is shorter than the coherence time τ_c of the stellar light source, the signal-to-noise expression is multiplied by $2\tau_j/\tau_c$, and becomes

$$\mathrm{SNR} = \frac{r}{2} V(b)^2 \sqrt{2\tau_j \Delta T}\,. \tag{1.22}$$

In this regime, the signal-to-noise ratio (SNR) is no longer independent of the optical bandpass, and will instead decrease with spectral filtering, due to the rate r of photoevents collected being reduced. Faster photon detectors with shorter timing jitter τ_j are no longer an advantage, as they sample a smaller fraction of the temporal photon bunching signal, and thus correspondingly a lower signal-to-noise ratio.

For these considerations, there has been a lack of development for spectral filtering in the efforts to revive stellar intensity interferometry so far [Foellmi, 2009], for the purpose of developing higher angular resolution imaging of stellar blackbody radiation sources like the stars [Dravins et al., 2010].

1.3 Blackbody Radiation

A thermal blackbody is a physical object which completely absorbs all incident radiation [Planck, 1900]. It also emits blackbody radiation at thermal equilibrium with its density of states $\rho(\nu)$, or the number of modes per unit frequency per unit volume [Fox, 2006], being described by

$$\rho(\nu) = \frac{8\pi}{c^3}\nu^2\,, \tag{1.23}$$

with each mode having an average energy $\langle E \rangle$ as defined by the individual photon energy multiplied with the probability of mode occupation described by

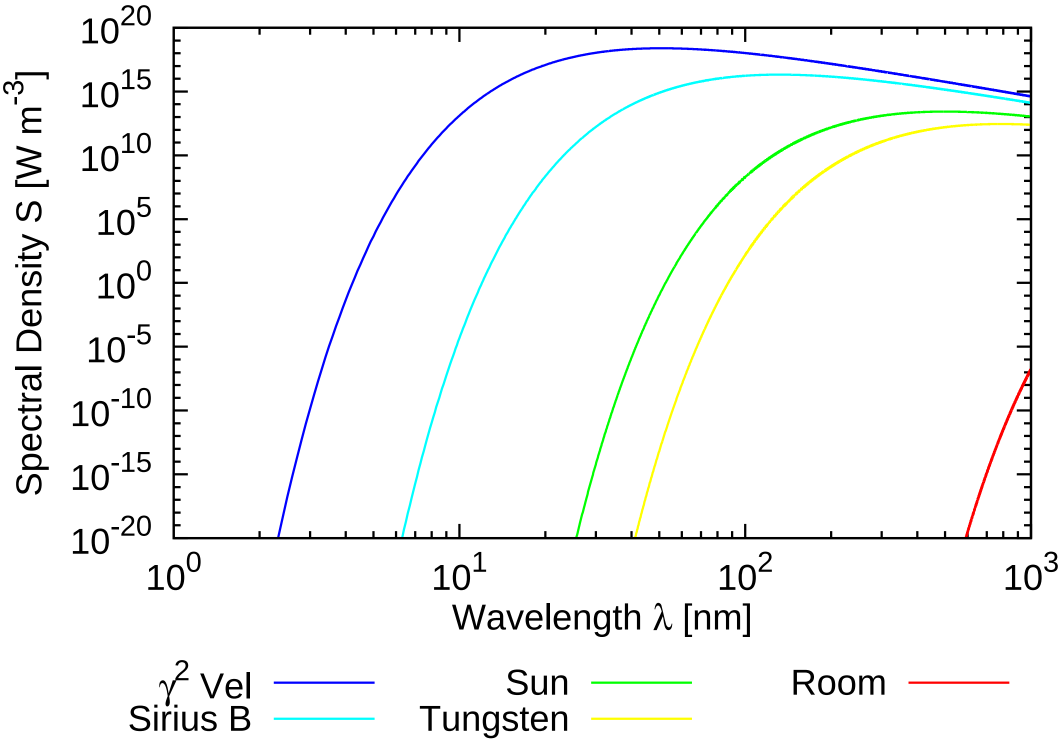

Figure 1.2: The ideal spectral density behaviour of some thermal blackbodies are shown here. The brightest Wolf-Rayet star is γ^2 Vel, with a surface temperature of 57000 K, and is a natural laser candidate [Dravins & Germanà, 2008]. Sirius is the brightest binary star system in the night sky, with its white dwarf component having a surface temperature of 22000 K emitting significant ultraviolet contribution [Allen, 2000]. The Sun has a surface temperature $T = 5800\,\mathrm{K}$, peaking in the green wavelengths which the human eyesight is most sensitive to. Tungsten filaments have a melting point of 3700 K, which is why filament bulbs appear orange. Blackbodies at room temperature of 300 K have negligible emissions in the visible spectrum.

the Bose-Einstein distribution

$$\langle E \rangle = h\nu \cdot \frac{1}{e^{h\nu/k_B T} - 1} \,. \tag{1.24}$$

Thus the power distribution emitted by such a blackbody surface with emissivity ϵ, per unit frequency per unit volume, can be described by the spectral density

$$S(\nu, T) = \frac{\epsilon 8\pi h\nu^3}{c^3} \cdot \frac{1}{e^{h\nu/k_B T} - 1} \,, \tag{1.25}$$

which is also known as the Planck radiation formula, with some representative temperatures and corresponding spectral density distributions illustrated in Fig. 1.2.

The radiation that can be extracted from blackbody sources through linear filtering process can be considered as thermal light, where linear filters include spectral filters, polarisers, lenses, mirrors and gratings [Mandel & Wolf, 1995].

Although a smaller telescope aperture will reduce the signal-to-noise ratio as seen in Eqn. 1.21, the aperture diameter b must first be shorter than the coherent length b_0 of the stellar light source, in order to resolve and probe the spatial correlation behaviour. Similarly, although having the histogram bin width Δt (limited by the detector timing jitter) to be shorter than the coherence timescale τ_c of the stellar light source will reduce the signal-to-noise ratio as described by Eqn. 1.22, this condition is required to resolve and thus probe the temporal correlation behaviour of the stellar light source.

Therefore, in order to investigate the possibility of stellar light sources exhibiting temporal coherence properties beside blackbody behaviour, this thesis proposes developing the instrumentation and experimental technique for narrowband spectral filtering to increase the coherence time of stellar light sources sufficiently to match photon detectors with high timing resolution. Such that we may be able to resolve and thus probe their timing correlation profiles, and apply towards astrophysical scenarios which will be briefly discussed in the concluding outlook chapter.

Chapter 2

Probing Blackbody Radiation: the Sun

The previous chapter highlighted the lack of spectral filtering in Hanbury-Brown & Twiss interferometry [Davis et al., 1999; Foellmi, 2009; Hanbury-Brown, 1974] due to the signal-to-noise ratio being independent of the optical bandpass as shown in Eqn. 1.21, for the regime where the detectors do not have sufficient timing resolution to probe the coherence timescale of blackbody radiation and thus unable to investigate its timing correlation behaviour.

Light from thermal blackbody radiators such as the stars exhibit photon bunching behaviour at sufficiently short time-scales. However, with available detector bandwidths, it is difficult to directly resolve this bunching signal for intensity interferometry with sufficient statistics in astronomy, nor to probe for stellar objects with temporal coherence properties other than the blackbody characteristic photon bunching behaviour [Fox, 2006].

In this chapter, we present an experimental technique to increase the temporal photon bunching signal in blackbody radiation via narrowband spectral filtering of the light source. Our measurements reveal strong temporal photon bunching in light from blackbody radiators, including the Sun.

Statistical intensity fluctuations from stationary thermal light sources formed the basis of the landmark experiments by Hanbury-Brown & Twiss [1956a, 1957, 1958], where correlation measurements between a pair of photodetection signals were used to assess both temporal and spatial coherence properties of light fields. The explanation for these fluctuations as a photon bunching phenomenon, as compared to a Poissonian distribution which describes coherent laser light, was a major contribution for the development of the field of quantum optics [Glauber, 1963].

Hanbury-Brown & Twiss [1954] developed their observations into a spatial intensity interferometer which allowed them to infer stellar angular radii from the coherence properties of star light over relatively large baselines of 188 m [Hanbury-Brown, 1974]. Since a key quality of any telescope system is its angular resolution, given by its real or virtual aperture, they managed to carry out these measurements with an unprecedented accuracy.

While stellar amplitude interferometry has evolved to become a standard technique to increase the effective angular resolution of radio telescope arrays, the angular resolution of the Hanbury-Brown–Twiss approach is still unmatched by conventional diffraction-limited optical telescopes. It is also very challenging to reproduce with Michelson interferometry due to the required sub-wavelength optical path length stability [Davis et al., 1999]. Such setups involve remote locations for observatory sites to reduce atmospheric turbulence [Dravins et al., 1997], as well as expensive and complicated adaptive optics to augment the measurable sensitivity by suppressing optical noise [Millour, 2008]. This results in the limited adoption of the comparatively simple optical intensity interferometry technique has not really found widespread adoption in the observation of celestial objects [Allen, 2000].

2.1 Temporal Photon Bunching

Temporal photon bunching, or the tendency for photons to cluster together on a short time-scale, has been consistently observed from narrow-band quasi-thermal light sources such as low pressure glow discharge lamps [Martienssen & Spiller, 1964; Morgan & Mandel, 1966], and laser beams which are passed through a rotating ground glass to randomise the optical phase in time [Arecchi, 1965; Asakura, 1970; Estes et al., 1971; Gonsiorowski & Dainty, 1983; Harwalkar et al., 1983]. Using Doppler broadened laser light to simulate thermal light characteristic correlations will be discussed in chapter 4.

Photon bunching in time for stationary fields is quantified by a second order correlation function $g^{(2)}(\tau)$, which is the probability of observing a second photodetection event at a time τ after a first one, normalised to the probability of an uncorrelated detection [Glauber, 1963; Mandel & Wolf, 1995; Saleh & Teich, 2007]. Optical modes in thermal states are the textbook example where $g^{(2)}(0) = 2$, with the characteristic behaviour [Fox, 2006] of other states being:

- Anti-bunching: $g^{(2)}(0) = 0$, e.g. atoms and molecules, quantum dots
- Random: $g^{(2)}(0) = 1$, e.g. coherent lasers, uncorrelated independent sources
- Bunching: $g^{(2)}(0) = 2$, e.g. blackbody radiation
- Special case: $g^{(2)}(0) > 2$, e.g. correlated photon pairs

Blackbody radiation would therefore be the obvious choice for observing photon bunching, if it were not for the short coherence time associated with its spectral properties.

In a scenario where spatial coherence effects are neglected, the second order temporal correlation function for light fields can be written as

$$g^{(2)}(\tau) = 1 + |\gamma(\tau)|^2 , \tag{2.1}$$

where $\gamma(\tau)$ is the complex degree of coherence, or the normalised self-coherence of the stationary light field with $\gamma(0) = 1$, which is proportional to the Fourier transform of the spectral density $S(\nu)$ of the light field [Mandel & Wolf, 1995; Planck, 1900]. For well-defined spectral densities and coherence functions, meaningful coherence times τ_c can be defined, which are reciprocal to a characteristic frequency width $\Delta\nu$ of the spectral distribution $S(\nu)$:

$$\tau_c = \frac{1}{\Delta\nu} . \tag{2.2}$$

For blackbody light sources in the optical regime, the coherence time τ_c given by Planck's law is on the order of 10^{-14} s, which is much shorter than the best timing resolution τ_j of a few 10^{-11} s of existing photodetectors. As shown by Scarl

[1968], the observable excess from uncorrelated pair detections, $g^{(2)}(\tau = 0) - 1$, scales as

$$g^{(2)}(\tau = 0) - 1 \propto \tau_c/\tau_j \,, \tag{2.3}$$

and is thus only significant when the coherence time τ_c of the source is of the order of the detection timing response τ_j. As an estimate, consider Sunlight which spans the visible spectrum, with a spectral range $\Delta\nu$ spanning from approximately 450 nm (blue) to roughly 650 nm (red), or about 200 THz wide which corresponds to a coherence time τ_c of only 5 fs.

Therefore, empirical observation of temporal photon bunching from blackbody light sources has been extremely difficult, with only recent breakthroughs by using two-photon absorption in semiconductors [Boitier et al., 2009], and in ghost imaging research using a narrowband Faraday anomalous dispersion optical filter [Karmakar et al., 2012; Liu et al., 2014].

In the following section, we present a narrowband spectral filtering technique that significantly increases the observed photon bunching signature from a blackbody light source, such that intensity interferometry techniques for observing astrophysical objects may become attractive again, with particular attention towards the previously neglected temporal component.

2.2 Narrowband Spectral Filtering

As with previous attempts to observe temporal photon bunching from blackbody radiation [Karmakar et al., 2012; Liu et al., 2014] which exhibit an ideal bunching signature of $g^{(2)}(\tau = 0) - 1 = 1$, we employ narrowband optical filtering of the light source to increase the coherence time τ_c, and use single photon detectors with low timing uncertainties. The experimental setup is illustrated in Fig. 2.1.

Firstly, light from different sources under investigation is coupled into a single mode optical fibre to enforce spatial coherence, because the temporal photon bunching signature $g^{(2)}(\tau = 0) - 1$ decreases from the ideal value of 1 by:

$$g^{(2)}(\tau = 0) - 1 \propto 1/M \,, \tag{2.4}$$

where M is the number of transverse modes [Glauber, 1963]. Spatial coherence is also required to optimise the filtering performance with both the diffraction grating and the Fabry-Pérot solid etalons.

The light is then collimated with an aspheric lens and sent through the first spectral filter, which is either an interferometric bandpass filter with a full width at half maximum (FWHM) of 3 nm centred at 546.1 nm to match the $6p7s\,^3S_1 - 6p6s\,^3P_2^0$ transition in a Mercury (Hg) discharge lamp, or a grating monochromator to serve as a tuneable filter for broadband continuous spectrum. While the interference bandpass filter is sufficient to select the discrete spectral emission lines in the Hg lamp, the grating monochromator had to be used for the blackbody light sources.

The core of the monochromator is a reflective diffraction grating blazed at 500 nm with 1200 lines/mm mounted on a motorised rotation stage. Light from the optical fibre (NA = 0.13) is collimated with an achromatic doublet (f = 30 mm), illuminating about 10^4 lines of the grating. The first diffraction order is

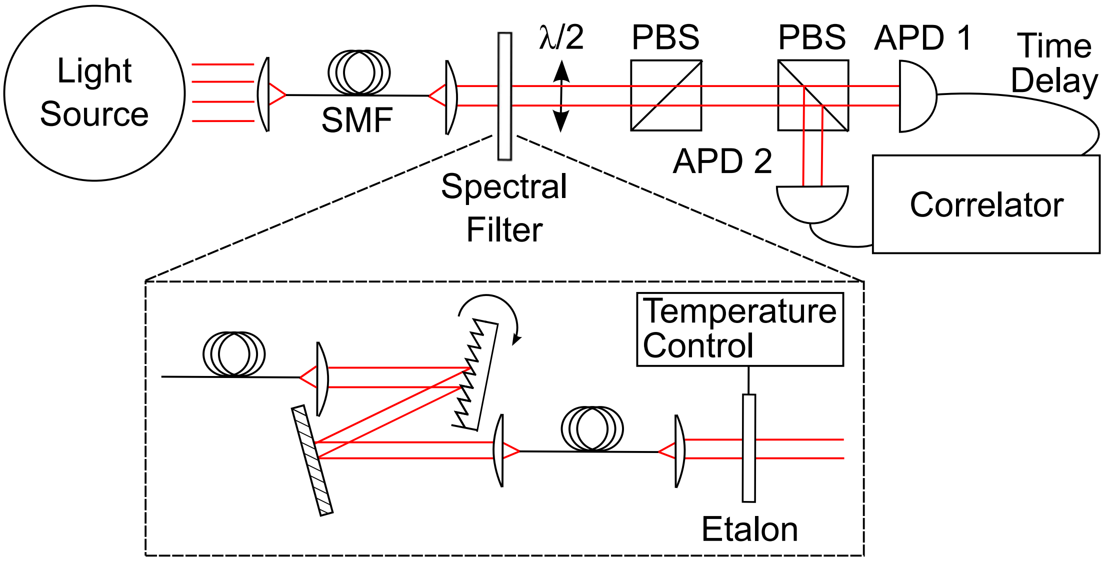

Figure 2.1: Setup to determine the temporal correlation $g^{(2)}(\tau)$ for wideband thermal light. The initial spectrum gets filtered to a narrow optical bandwidth such that the temporal decay of the second order correlation function can be observed with conventional single photon detectors in a Hanbury-Brown–Twiss experiment. We employ a combination of a grating and a temperature-tuned etalon as a spectral filter, and ensure spatial coherence in the setup by using single mode optical fibres (SMF).

imaged with another achromat of ($f = 30\,\mathrm{mm}$) into another single mode optical fibre. This arrangement acts as a tuneable narrowband filter in the visible regime, allowing to adjust for peak emissions of blackbody light sources. A test of the transmission of a narrowband laser source ($\lambda = 532\,\mathrm{nm}$) is shown in Fig. 2.2 (top part). The fit to a Gaussian transmission profile leads to an optical bandwidth of $0.122 \pm 0.002\,\mathrm{nm}$ (FWHM), which approaches the diffraction-limited resolution of about $0.06\,\mathrm{nm}$ as given by Eqn. 2.8, but still lower than the ideal bound by a factor of 2. We typically observe an effective transmission of narrowband light from single mode fibre to single mode fibre of $\approx 15\%$. The optical fibres used generally have Angled Physical Contact (APC) terminals, which is an 8° slant to the connector surface. This is to reduce back reflections by typically 60 dB, thus suppressing interference and noise.

In a second step, the light is passed through a solid etalon (thickness $d = 0.5\,\mathrm{mm}$) with flat parallel surfaces. The etalon has a free spectral range of $FSR = c/(2nd) = 205\,\mathrm{GHz}$, with a refractive index $n = 1.46$ [Heraeus, 2013] for the fused silica material (Suprasil311), and the speed of light c in vacuum. At $\lambda = 546\,\mathrm{nm}$, the free spectral range corresponds to $\Delta\lambda = \lambda^2/c \cdot FSR \approx 0.2\,\mathrm{nm}$, so that only one transmission order should fall within the transmission width of the grating monochromator.

Both surfaces of the etalon have dielectric coatings with an ideal reflectivity of $R \approx 97\%$ over a wavelength range from 390 nm to 810 nm, resulting in a transmission bandwidth $\Delta\nu$ of

$$\Delta\nu \approx FSR \cdot \frac{1-R}{\pi\sqrt{R}} \approx 2\,\mathrm{GHz}\,. \tag{2.5}$$

The central transmission frequency of the etalon is tuned by temperature, with a scaling rate of -4.1 GHz/K due to thermal expansion and temperature dependence of the refractive index [Ghosh, 1997; Schott, 2007, 2010]. A temperature stability of $\pm 5\,\mathrm{mK}$ over the measurement duration of several hours ensures that the etalon stays on a specific wavelength. The etalons are temperature stabilised via a proportional-integral-derivative (PID) control loop feedback, using a set of 4 high power resistors as the heating element and a 10 kOhm thermistor to provide the temperature feedback.

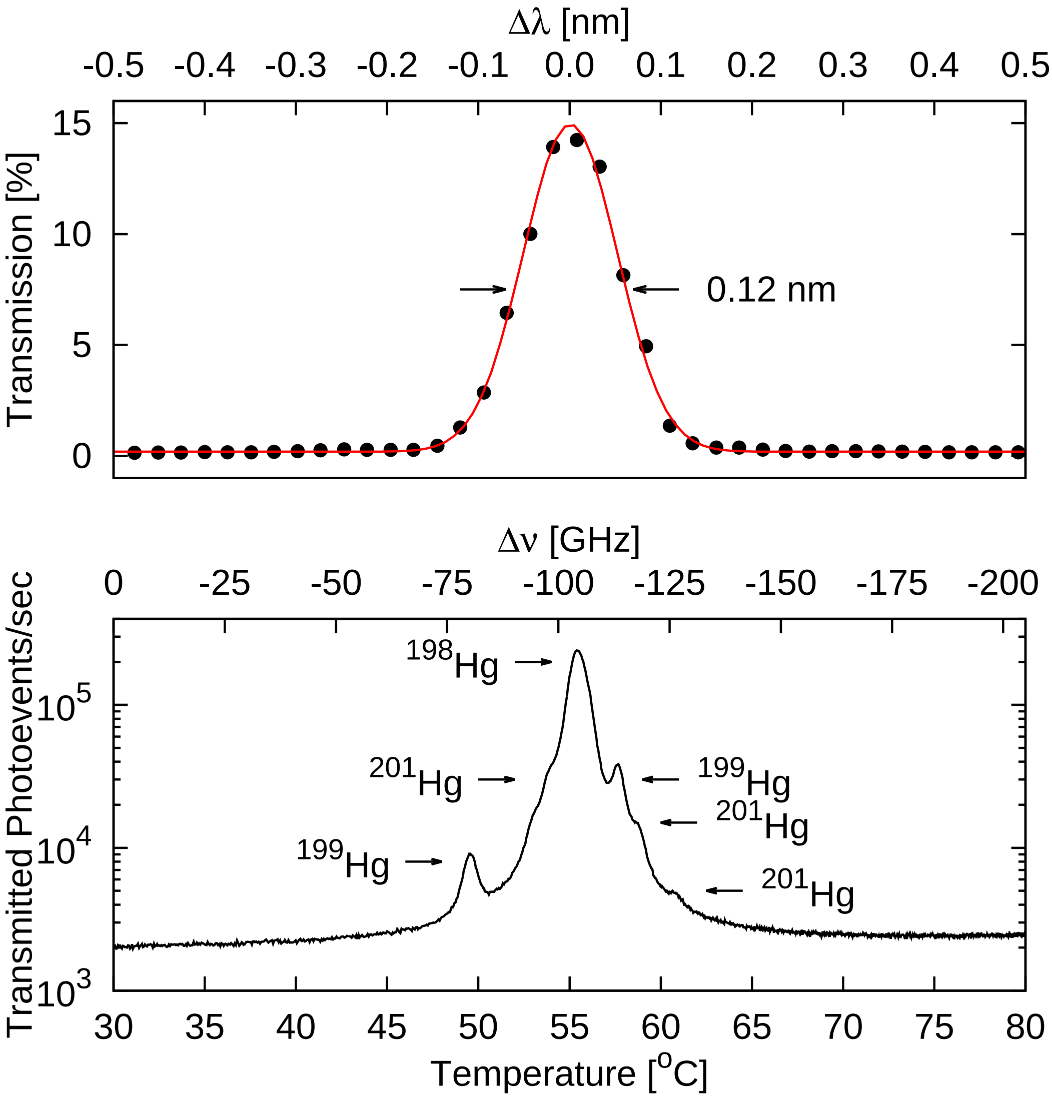

Figure 2.2: (Top) Transmission profile of grating monochromator. The solid line is a fit to a Gaussian profile to measurements for different grating angles (symbols), resulting in a full width at half maximum (FWHM) of 0.122±0.002 nm. (Bottom) Transmission of Hg light near 546 nm for the $6p7s\,^3S_1 - 6p6s\,^3P_2^0$ transition, which is the Fraunhofer "e" line, through the temperature-tuned etalon with 2 GHz bandwidth. The hyperfine structure for different isotopes is partially resolved, as identified in [Sansonetti & Veza, 2010].

Temperature tuning allows the etalon to be always used under normal incidence, which avoids both frequency walk-off [Green, 1980] as well as spatial distortion [Park et al., 2005]. To demonstrate the resolving power of this device, we tuned the peak transmission across the various spectral lines from a Hg gas discharge lamp at 546.1 nm, revealing a partially resolved hyperfine structure for different isotopes with non-zero nuclear spins (see Fig. 2.2, bottom part).

A Glan-Taylor polariser following the etalon then selects a well-defined linear polarisation mode for the photons, with the same rationale of minimising the number of modes ending up in the temporal correlation setup. A half-wave plate ($\lambda/2$) transforms the polarisation emerging from the grating/fibre combination such that there is maximal transmission through the Glan-Taylor polariser and finally the detectors.

The diffraction grating introduces polarisation effects to the input light, which transforms as it propagates through the optical fibres due to the birefringence induced largely by mechanical stress on the fibres, thus necessitating the use of the Glan-Taylor polariser and half-wave plate for mode selection and clean-up. The degree of polarisation P is given by [Loudon, 2000]:

$$P = \frac{|\bar{n}_x - \bar{n}_y|}{\bar{n}_x + \bar{n}_y}\,, \tag{2.6}$$

where $\bar{n}_x, \bar{n}_y$ are the number of photons in any pair of orthogonal polarisation planes, with P scaling from 0 for unpolarised light, to 1 for perfectly linearly polarised light, thus affecting the coherence of light according to:

$$g^2(0) = \frac{1}{2}(3 + P^2)\,. \tag{2.7}$$

This corresponds to the ideal peak $g^2(0)$ values ranging from 1.5 for unpolarised light to 2 for perfectly linearly polarised light.

A second Glan-Taylor polariser, rotated by ≈ 45° with respect to the polarisation direction of the first, works as a polarising beamsplitter in distributing the light onto two silicon avalanche photodetectors (APD) that provide detection timing signals to a correlator. The relative orientation of the two polarisers allows for the balancing of the photodetection rates to optimise the integration time, and also helps to suppress the optical crosstalk between the two APDs due to hot carrier recombination in the devices upon detection which would otherwise introduce false coincidence events [Kurtsiefer et al., 2001].

Let the individual photoevent rates received by the two detectors be A and B individually, so that $A + B = I$, the original intensity, before the beamsplitter, assuming no losses. Thus the coincidence rate observed will be proportional to $A(I - A)$, with a maximum rate when its differential with respect to A is zero, i.e., $I - 2A = 0$. This implies that the maximum coincidence rate occurs when $A = I/2 = B$, or a balanced single-photoevents rate between the two photon detectors, for optimal efficiency in coincidence measurements.

Note that the choice of Calcite Glan-Taylor as polarisation elements is due to its broadband performance (350 nm to 2300 nm), and a high extinction ratio of greater than 10^5:1 for the transmission beam, although its disadvantage is that the reflected beam through the escape window is not purely polarised.

The temporal correlation was carried out with a digital sampling oscilloscope (4 GHz analog bandwidth, 40 Gsamples/sec, LeCroy) that can measure and histogram detection timing differences between two photon detector (APD) events with a software-assisted interpolated timing uncertainty below 100 fs [Lecroy, 2011].

To assess the overall timing uncertainty with the detector/correlator combination, we exposed two different avalanche photodetector (APDs) sets to photon pairs generated by spontaneous parametric down conversion (SPDC) with a coherence time τ_c below 100 fs [Hong et al., 1987]. The resulting temporal correlations shown in Fig. 2.3 reflects the overall timing resolution of the system. For APDs with a deep conversion zone (C30902S, Perkin-Elmer, passive quenching), the coincidence distribution appears roughly Gaussian, with 1.2 ns FWHM. Since the temporal photon bunching signature $g^{(2)}(\tau)$ of the light field under investigation needs to be convolved with this detector response, we would observe a significant reduction of the photon bunching peak with these detectors. A second set of APDs, based on thin conversion zones (type PDF, Micro Photon Devices, active quenching), leads to a much better localised coincidence distribution with 40 ps FWHM, although a significant fraction (roughly half) of the distribution shows a tail with timing differences up to 500 ps.

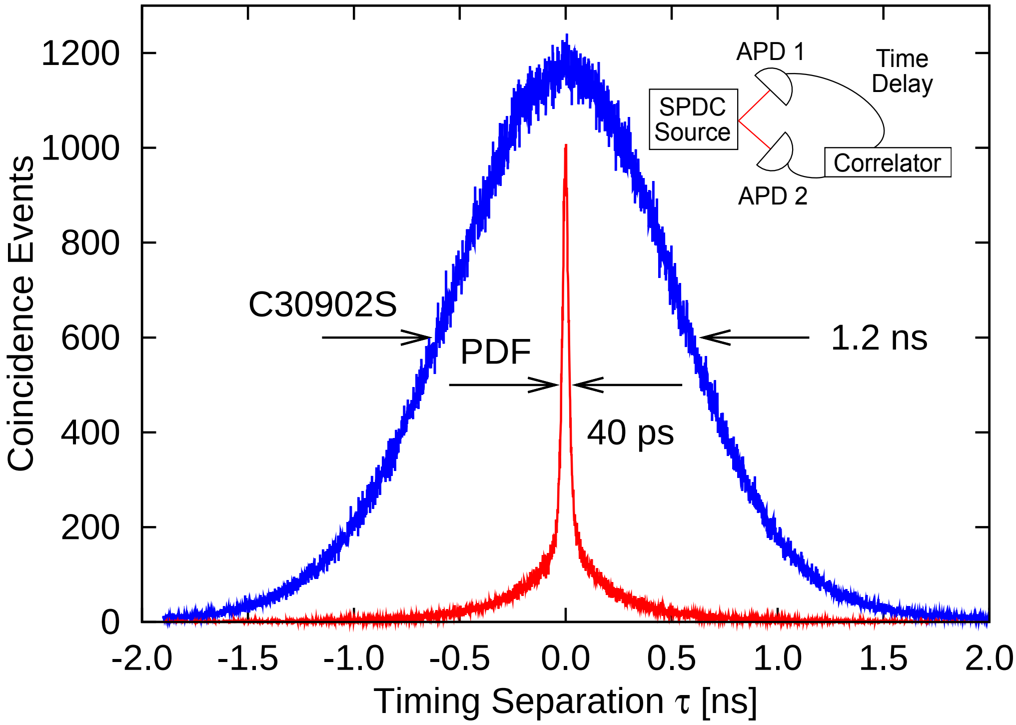

Figure 2.3: Comparison of timing jitter between two actively quenched thin avalanche photodiodes (PDF), and two passively quenched deep avalanche photodiodes (C90302S) by photon pair detection from light generated by spontaneous parametric down conversion (SPDC) with a coherence time τ_c below 10 ps.

We will revisit the temporal response of the actively quenched APDs in the next chapter, to better understand the difference between the measured and ideal photon bunching peak values, paying particular attention to the long tail structure which upon fitting suggests about 50 % proportion of the timing jitter distribution, nearly equal in statistical weight to the central peak structure with FWHM, which is the common understanding of detector timing uncertainty, of approximately 40 ps.

2.2.1 Diffraction Grating

Although in principle a prism could also be used to disperse optical light, its resolution is determined by its Abbe number V_d [Hecht & Zajac, 1997] which indicates the level of dispersion, and is thus limited by the refractive index of the glass substrate, which is mostly $n < 2$.

A reflective diffraction grating is instead chosen, specifically the ruled (blazed) design so as to increase the coupling efficiency as more of the input optical light would be in the first diffraction order, as opposed to holographic gratings with reduced ghosting nor Echelle gratings with low periodicity.

Grating Monochromator

The diffraction grating is configured as a grating monochromator [Fastie, 1952], in order to serve as a narrowband spectral filter (FWHM = 0.12 nm) that is tuneable over a broad spectrum. It is worth noting here for practical considerations, that laser-line bandpass filters with FWHM of around 2 nm can easily cost a few hundred dollars off-the-shelf upwards to over a thousand dollars for custom specifications, and are not as easily tuneable.

The resolvance R, or chromatic resolving power, of the diffraction grating can be described by

$$R = \frac{\lambda}{\Delta\lambda} = mN \,, \tag{2.8}$$

where m is the diffraction order and N is the total number of slits illuminated by the incident beam. The order $m = -1$ is used due to the blazed design, with N given by the grating slit separation $\frac{1}{1200}\,\text{mm} \approx 833\,\text{nm}$, with a Gaussian beam of $1/e^2$ width $= 2 \times \text{NA} \times \text{EFL} = 7.8\,\text{mm}$.

The optical dispersion by the grating can be characterised as

$$a(\sin I + \sin D) = m\lambda \,, \tag{2.9}$$

with the slit separation a, incident angle I and diffracted angle D. However, a more convenient form for the grating monochromator setup used in this thesis is

$$m\lambda = 2 \times a \times \cos\phi \times \sin\theta \,, \tag{2.10}$$

where ϕ is half the included angle between the incident and diffracted rays which defines the relative positions of the input and collection optical fibres/lenses, and θ is the grating angle relative to the zeroth order position and so controlled, and tuned, by the motorised rotational stage.

Coupling Efficiency

To optimise the transmission performance of the grating monochromator as a spectral filter, we must understand the dependence of the coupling efficiency between the input and collection optical fibres on the empirical degrees of freedom, and thus design the instruments and alignment protocol accordingly to compensate.

The mode-matching conditions [Horton & Bland-Hawthorn, 2007; Shaklan & Roddier, 1988] and thus transmission performance between the input and diffracted modes of light can be ideally described as

$$T = \frac{[\int (E_1 E_2^*) \cdot \mathrm{d}A]^2}{\int (E_1 E_1^*) \cdot \mathrm{d}A \cdot \int (E_2 E_2^*) \cdot \mathrm{d}A} \,. \tag{2.11}$$

Translated to the experimental context, let us interpret the physical degrees of freedom in terms of axial (z-axis), lateral (x, y-axes), tilt (θ, ϕ) and beam shape of the incident and collection optics.

For the axial degree of freedom, z-translation stages with micro-metre precision and 1.5 mm travel are used to focus each lens with its corresponding fibre, to first collimate the resultant beams and then adjust to compensate for the axial offset. This is a reason why the input and collection optics are symmetric, in using the same specifications of optical fibres and lenses.

With regards to lateral offsets, x-y translation stages (Thorlabs ST1XY-A) are used to mount the optical fibres, allowing for adjustments of the fibre tip positions with respect to the lens. The vertical adjustment (knob) is particularly susceptible to drifts, perhaps due to internal springs or threading against the weight of the lens, thus requiring minor realignment every few days.

Tilt mounts are used to hold the mirror and grating, to allow alignment of the input and collection beams to be collinear and anti-parallel, instead of just spatial overlaps at a position. This degree of freedom is more sensitive than the axial and lateral, albeit stable. It is thus advisable to use pinholes to reduce the beams to roughly 1 mm in diameter for easier alignment and overlaps at multiple positions.

The most tricky condition to compensate for is the spatial mode mismatch due to the astigmatism caused by the diffraction grating, which transforms the the incident Gaussian profile into an elliptical structure when diffracted. This is partially corrected for by defocusing the collection lens to transform the collection beam shape. While worse performing than using toroidal mirrors, anamorphic prisms or cylindrical lenses, such a correction method is much simpler to align and compensate for, as well as cheaper and compact.

2.2.2 Etalon Tuning

Solid etalons are selected due to their compact form factor, the lack of moving parts and thus mechanical stability. The choice of the etalon substrate to be Suprasil311, a class of fused silica, is made similarly due to its thermal and mechanical performance, along with the lack of fluorescence which N-BK7 suffers from in the blue wavelengths.

Temperature control is used to tune the transmission wavelength, so as to avoid frequency walk-off effects [Green, 1980], alignment complications and mechanical stress. For safety and practical considerations in avoiding thermal convection air currents, there are bounds on the temperature range which should be operated in, roughly from room temperature of around 25°C to near 90°C.

The transmission FWHM of the grating monochromator restricts the minimum free spectral range (FSR) of the etalon and correspondingly the maximum substrate thickness. The etalon tuning rate, or wavelength change per unit temperature difference, requires the temperature range to cover at least one full FSR in order to matching the grating transmission with the etalon, and thus have complete access to the effective joint transmission spectrum.

The optical dispersion $n(\lambda)$ behaviour of Suprasil311, or the dependency of its refractive index on wavelength, can be described by the empirical Sellmeier Dispersion Equation [Ghosh, 1997]:

$$n^2(\lambda) = 1 + \frac{B_1\lambda^2}{\lambda^2 - C_1} + \frac{B_2\lambda^2}{\lambda^2 - C_2} + \frac{B_3\lambda^2}{\lambda^2 - C_3}\,, \tag{2.12}$$

which is used in conjunction with the empirically determined coefficients for the specific glass material as shown in Tab. 2.1, where λ is considered in vacuum.

Sellmeier Coefficients	**Empirical Values**
B_1	$7.99316057 \times 10^{-1}$
B_2	$3.04794111 \times 10^{-1}$
B_3	$8.85442870 \times 10^{-1}$
C_1	$5.34990808 \times 10^{-3}$
C_2	$1.47511317 \times 10^{-2}$
C_3	9.66383219×10^{1}

Table 2.1: Suprasil311 Sellmeier coefficients provided by Schott AG.

To better understand the performance of the substrate under temperature control, consider the derivative $\frac{dn}{dT}$ of the Sellmeier equation with respect to temperature, with simplification by dropping negligible contribution terms:

$$\frac{\mathrm{d}n_{abs}(\lambda, T)}{\mathrm{d}T} = \frac{n^2(\lambda, T_0) - 1}{2n(\lambda, T_0)} \left(D_0 + 2D_1\Delta T + 3D_2\Delta T^2 + \frac{E_0 + 2E_1\Delta T}{\lambda^2 - \lambda_{TK}^2} \right) , \tag{2.13}$$

with a reference temperature $T_0 = 20°\mathrm{C}$, a temperature difference $\Delta T = T - T_0$ and a vacuum wavelength λ in μm, and the corresponding Sellmeier coefficients in Tab. 2.2.

Sellmeier Coefficients	**Empirical Values**
D_0	2.18×10^{-5}
D_1	2.45×10^{-8}
D_1	-2.72×10^{-11}
E_0	2.31×10^{-7}
E_1	2.21×10^{-10}
λ_{TK}	$0.235\,\mu\mathrm{m}$

Table 2.2: Suprasil311 derivative coefficients also provided for by Schott AG.

The mean thermal linear expansion of a substrate material is denoted by the coefficient α. Provided by Heraeus Gmbh, for temperature range of 0°C to 100°C, the Suprasil311 material $\alpha = 5.1 \times 10^{-7}\,\mathrm{K}^{-1}$.

The dependency, or tuning rate, was empirically determined to be $-4.1\,\mathrm{GHz/K}$, which is sufficient to cover one full free spectral range, e.g. about 24°C increase in the heating up of the etalons in order to contribute $-0.1\,\mathrm{nm}$ in the transmitted wavelength. The periodicity of the etalon transmission behaviour allows us to access increments in transmission wavelengths, conditional only on the ability to scan across an entire free spectral range (FSR).

2.2.3 Broadband Etalon Coating

The etalons are designed to operate across the visible spectrum, from 390 nm to 810 nm, as indicated in Fig. 2.4, to have the versatility to examine a variety of light sources. This is compatible with the use of the diffraction grating monochromator as a first-stage spectral filter tuneable across the optical regime.

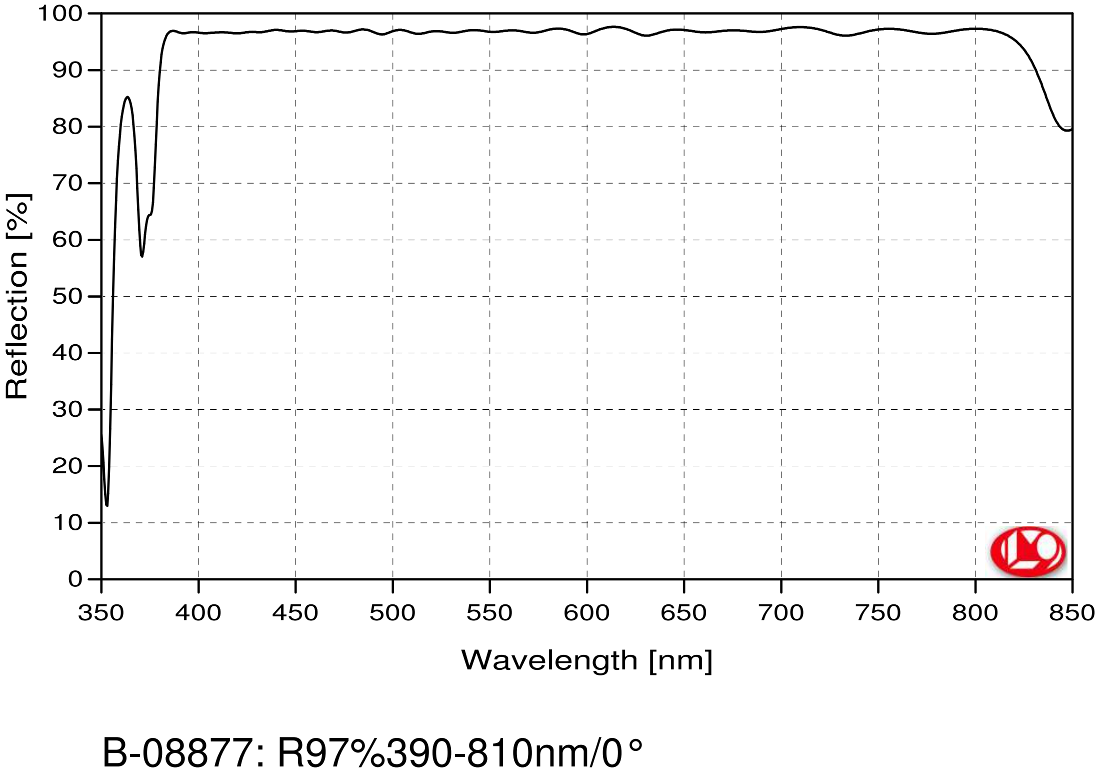

Figure 2.4: The reflectivity R = 97 % coating on the etalons, designed to perform at normal incidence, for light from 390 nm to 810 nm to cover the full visible spectrum. The plot is a technical document provided by Laseroptik Gmbh, the company that provided the etalon substrates and coatings.

2.2.4 Photon Detector

Fast APDs have thin depletion zones to improve their timing jitter, but thus suffer in quantum efficiency. To compensate, some designs incorporate an internal cavity to enhance the optical field [Ghioni et al., 2008] but results in a long 'tail' as seen in Fig. 2.5. We will revisit this APD performance in the next chapter.

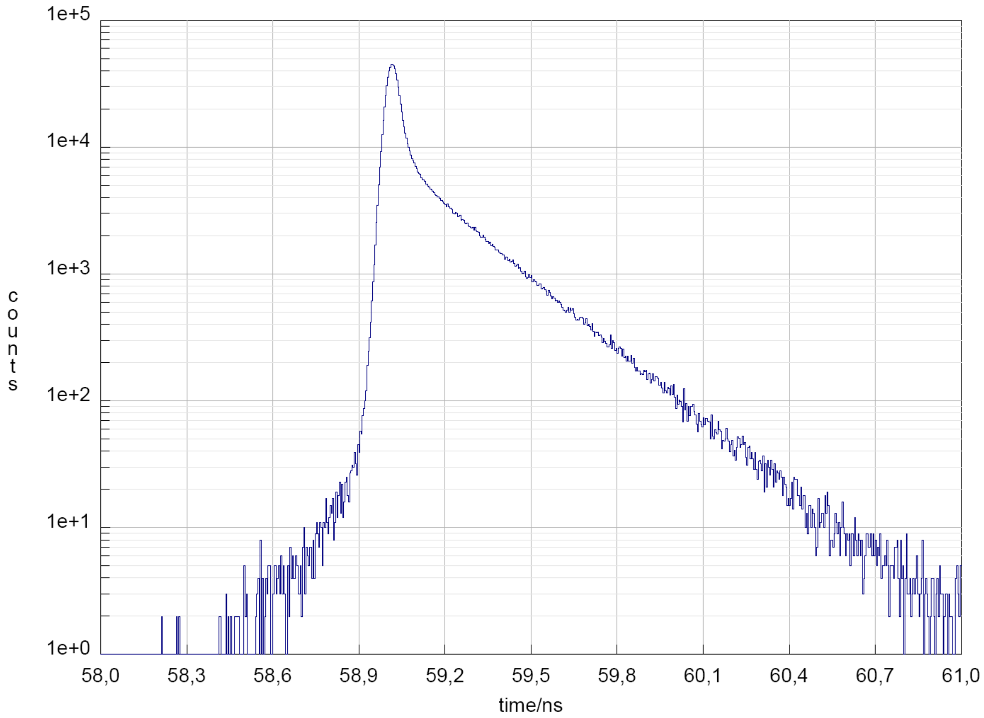

Figure 2.5: This is the instrument response function (IRF) provided by the manufacturer Micro Photon Devices, that describes the timing response of their actively quenched silicon avalanche photon detector module that is used in this thesis.

2.2.5 Digital Oscilloscope

While the input optical signals are measured by the photon detectors (APDs), the electrical signals generated by the APDs are in turn time-stamped by a digital oscilloscope for further statistical analysis.

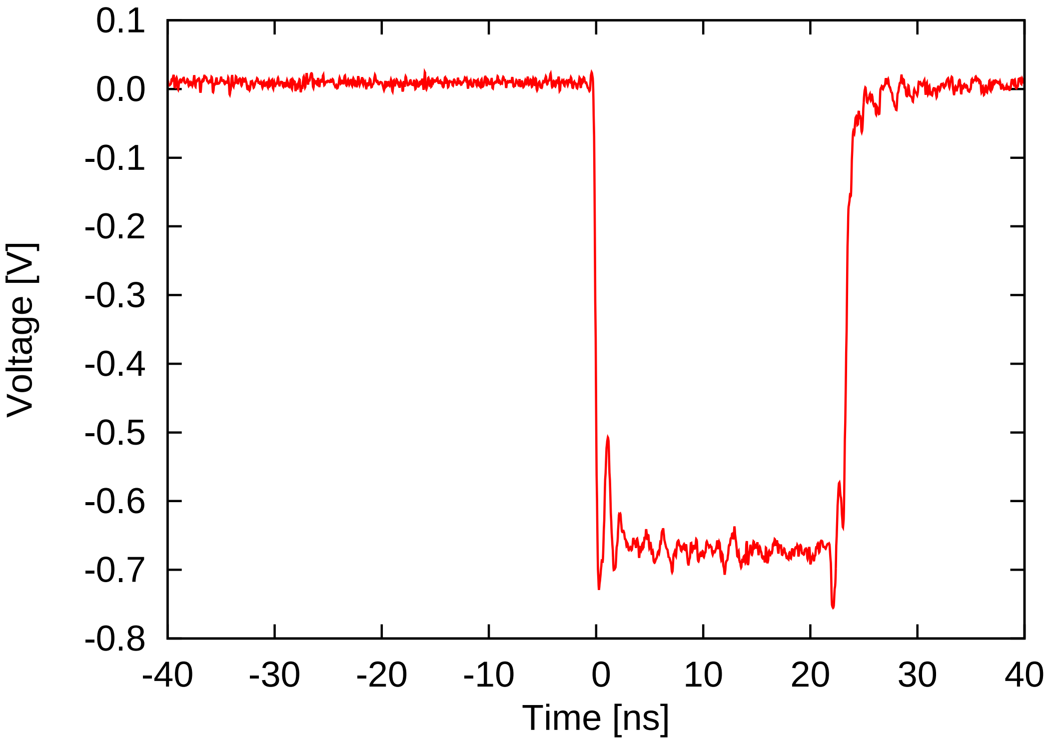

Figure 2.6: This pulse signal is generated by the NIM output of the actively quenched APDs used, as measured by the oscilloscope to be about -700 mV in depth and 20 ns wide, with each pulse corresponding to a photoevent detection.

The oscilloscope used is a Lecroy 640Zi Waverunner model with 4 GHz bandwidth and a sampling rate of 20 Gsamples/s. As a time-stamp, it does not flag and process all the APD events, but only consecutive events that make up a coincidence, with an undetermined dead-time for data processing. This means a significant fraction of the events are not registered, a trade-off for the timing resolution of a few ps. These are some of the parameter settings used and their considerations.

Photon detector output signal

We chose to use the NIM (Nuclear Instrumentation Module standard) output signal, as shown in shown in Fig. 2.6, of the photon detector (APD) for time-stamping the photoevents, rather than the TTL (Transistor-Transistor Logic) positive voltage signal output from the APD. This is because the NIM signal has better timing precision in the tens of ps, as opposed to the TTL signal with about 250 ps timing resolution stated by the manufacturer. The timing uncertainty from a signal is defined by its leading edge, i.e., the steeper the gradient of the leading edge, such as the NIM pulse with roughly 1 ns only, the higher the timing accuracy.

The signal is directed to a 50 Ω terminal on the oscilloscope instead of 1 MΩ, out of impedance matching considerations to minimise electrical signal reflection and to optimise the signal strength transferred into the oscilloscope. This can be considered as the electronic analogue to the more familiar optical situation of light reflecting at the interface between mediums with different refractive index.

However, the straightforward LEMO connectors/cables, that are common for use with NIM signals, are actually fairly lossy and susceptible to electrical noise, and therefore advisable to use adaptors instead with the following BNC cables.

Coaxial cable

The data signals were transferred from the detectors to the oscilloscope using RG-58/U coaxial cables, using BNC (Bayonet Neill-Concelman) connectors, with a characteristic impedance of 50 Ω. The coaxial design provides shielding, similar in principle to a Faraday cage, which suppresses electrical noise and signal degradation, and thus a common choice for data cables.

An electronic delay is introduced in the trigger arm during coincidence measurements due to the oscilloscope dead-time, just as the use of a beamsplitter is to compensate for the APD dead-time. This is achieved by connecting additional BNC cables, keeping in mind the translation scale of 1 ns signal delay for every 20 cm of cable length, similar to the effective ‘speed’ of the light signal propagating in optical fibres.

Coincidence measurements are performed between channels 2 and 3 to double the maximum sampling rate to 40 Gsamples/s. This is because these two channels are paired, as are channels 1 with 4, with the particular configuration differing between oscilloscope models.

Oscilloscope settings

The trigger levels for both the trigger and qualifier are set near the mid-point of the leading edge, i.e. trigger level of $-350\,\text{mV}$ at the negative slope. The vertical scale is adjusted such that the NIM signal maximises the use of the screen, and therefore the ADC (analog-to-digital converter) range, at $100\,\text{mV}$ per division across 8 vertical divisions with a $350\,\text{mV}$ offset, so as to optimise the sample points available for interpolation of gradient and thus the timing position. The triggers are further constrained with a hysteresis of 0.5 vertical division, so as to reject minor noise contributions smaller than the hysteresis and avoid false triggers on the noise.

To perform the two-photoevent coincidence measurement, the "time@level operation" is chosen to identify pairs of trigger and qualifier signals, corresponding to a photoevent signal each, and then to measure their mutual timing separation. A horizontal depth of $6.3\,\text{ns}$ hold-off is chosen to reduce the waiting intervals without a temporal photon bunching signal, allowing for a faster reacquisition for the next coincidence event, and thus optimising the overall integration time.

The time@level measurements are grouped into a histogram of their timing separations, so as to extract the photoevent temporal correlation. 500 bins is chosen over a $20\,\text{ns}$ width across 10 horizontal divisions, in order to match the $40\,\text{ps}$ timing jitter τ_j of the APDs. This is because if the time-bin is smaller than the timing jitter, then the bunching signal is spread out over more bins which is inefficient. But if the bin is wider, then it increases the timing uncertainty instead.

The measurements are acquired in sequence mode instead of real-time, so as to avoid the processing time required to process and display the signal in real-time. The maximum of 5000 acquisition segments per sequence is used to optimise the collection rate, with 6400 sample points in the coincidence window and 2 active channels.

The processing required to display the input NIM pulses from both APD signals will significantly slow down the overall effective acquisition rate and thus should be switched off.

2.3 Results

Measurements of $g^{(2)}(\tau)$ were performed using three light sources: a low pressure Mercury (Hg) discharge lamp as a quasi-thermal light source, a radio frequency-driven Argon (Ar) arc discharge lamp to produce a plasma with a blackbody temperature $T \approx 6000\,\mathrm{K}$ as the thermal light source, and the Sun as a celestial thermal light source. Their respective spectral distributions are shown in Fig. 2.7.

Note that the red wavelengths in the Hg spectrum are due to the Argon buffer gas. Also, the Hg plasma/droplets have a tendency to drift over time, and thus require frequent repositioning of the discharge tube to compensate. Zinc or Sulphur powder may be used in the event of a minor accident to clean up the Mercury spill for disposal, as occurred during this experiment, and thus a supply should be maintained for safety considerations.

The optical filters were fixed to maximise transmission for the spectral lines

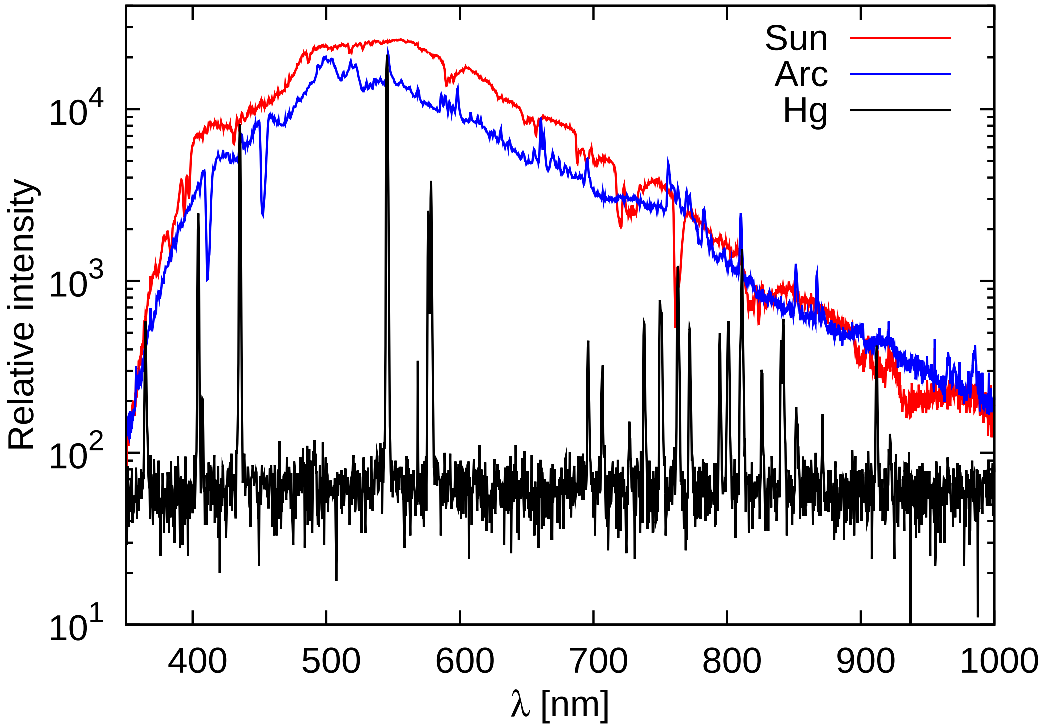

Figure 2.7: Spectrum of a Hg glow discharge lamp, an Ar arc lamp as a simulator of a stellar light source, and the Sun.

around 546.1 nm in the Hg spectrum. The resulting timing difference histograms are shown in Fig. 2.8.

To ensure proper normalisation of the resulting $g^{(2)}(\tau)$, we independently recorded pair events with a resolution of about 300 ps with a time stamp unit that, unlike the oscilloscope, does not exhibit a significant dead time, and found that $g^{(2)}(|\tau| \gtrsim 2\,\text{ns}) \to 1$. To extract a meaningful set of model parameters, we assumed a Lorentzian line shape for the spectral power distribution; this is mostly to reflect the approximate transmission function of the etalon.

A corresponding model function for the obtained pair rates in the histograms is described by

$$N(\tau) = a + b \cdot e^{-|2\tau/\tau_c|}\,, \tag{2.14}$$

where a, b capture the absolute event number and the degree of bunching respectively such that $g^{(2)}(\tau = 0) = b/a$, while τ_c represents a coherence time. The $g^{(2)}$ scale on the right side of diagrams in Fig. 2.8 refers to the absolute number of coincidence events after division by the fit parameter a.

For the Hg emission line at 546 nm from the low pressure glow discharge lamp, coincidence data was obtained over an integration time of 68 hours, with single detector rates of $115000\,\text{s}^{-1}$. The relatively large discrepancy between expected coincidences with the single rates and the observed coincidences is due to a dead time of the oscilloscope in this measurement. Photon detectors also introduce a dead time, during which no photoevent can be measured. The actively quenched APDs used here have a dead time of $\approx 80\,\text{ns}$, and the passively quenched models about $1.2\,\mu\text{s}$.

From the numerical fit, we find that $g^{(2)}(\tau = 0) = 1.79 \pm 0.01$ and an exponential decay with a characteristic coherence time of $\tau_c = 0.436 \pm 0.006\,\text{ns}$ at a reduced $\chi_r^2 = 1.51$. The photon bunching signature comes very close to the expected value of 2 for a thermal state, with the difference possibly due to the residual timing uncertainty of our photodetectors, particularly the long-tail structure noted earlier.

While the Doppler-broadened line width for individual transitions in Hg vapour at temperatures around 400 K is on the order of 235 MHz, the contributions of different hyperfine transitions from different isotopes result in a complex overall

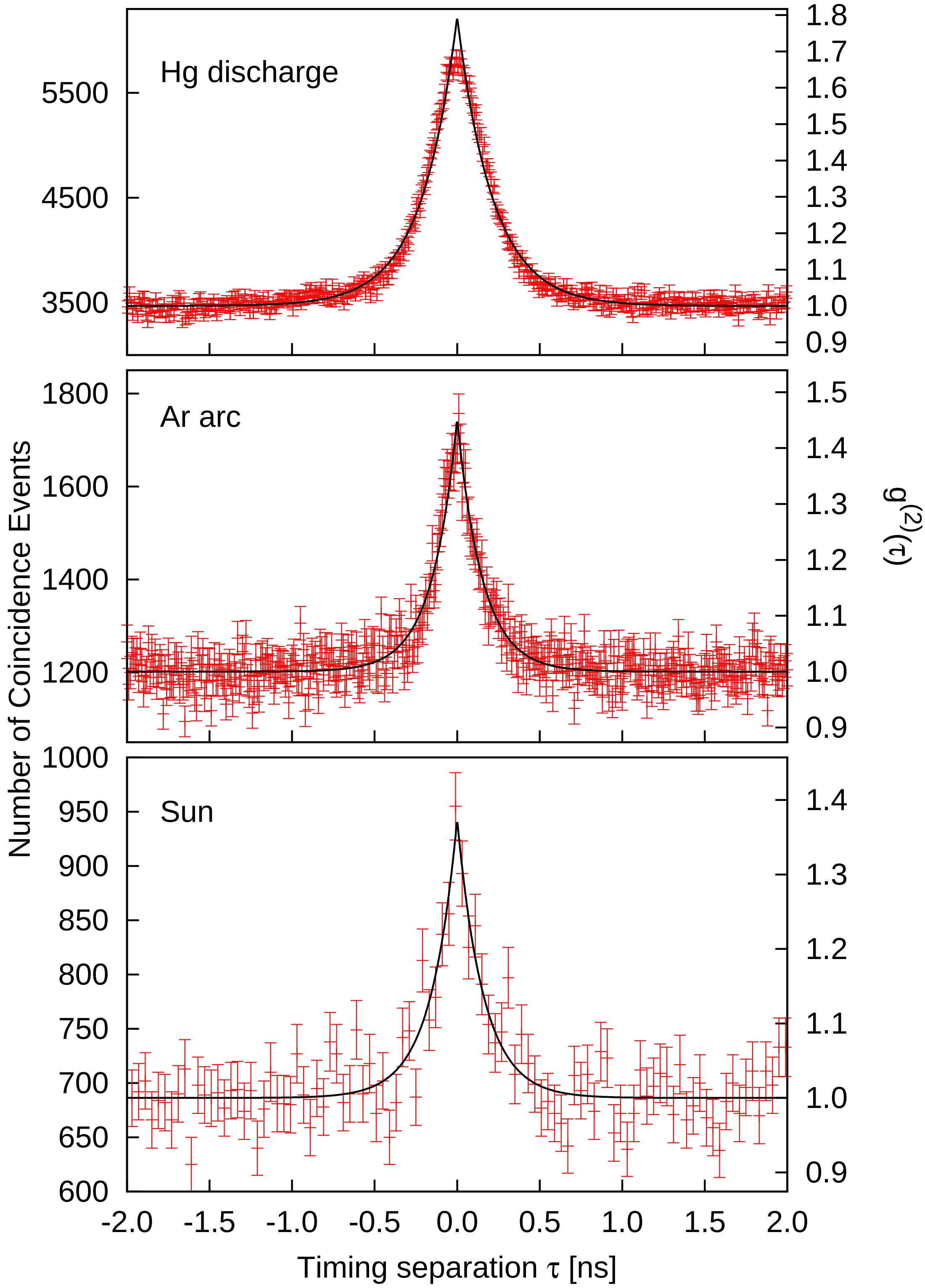

Figure 2.8: Intensity correlation function $g^{(2)}(\tau)$ from the three thermal light sources after spectral filtering. All light sources show a significant bunching at $\tau = 0$, and a decay time that is well-resolved with the avalanche photodetectors. Error bars indicate uncertainties due to Poissonian counting statistics.

line shape of several GHz width, out of which we select a reasonable fraction with the etalon. The Doppler broadening of a Gaussian profile centred at f_0, where m is the atomic mass of Hg, which is 3.3×10^{-25} kg, gives a broadened FWHM of

$$\Delta f_{FWHM} = f_0 \cdot \sqrt{\frac{8k_B T \ln 2}{mc^2}} \tag{2.15}$$

For the Argon arc discharge lamp, a wavelength of 540 nm was chosen to avoid contributions of a prominent peak at 546 nm, possibly caused by mercury traces in the plasma. We find that $g^{(2)}(0) = 1.45 \pm 0.03$ and a shorter coherence time $\tau_c = 0.31 \pm 0.01$ ns with a reduced $\chi_r^2 = 1.066$. The wider spectrum of the cut-out blackbody radiation makes the decay time shorter, so a peak reduction due to the detector response becomes more pronounced. Furthermore, residual transmission of the grating monochromator or stray light into other transmission peaks of the etalon may contribute to light that is not coherent with the main peak on observable time-scales, thus reducing the coherence time and the bunching signal.

We finally collected Sunlight into a single mode optical fibre with a coelostat, made up of a mirror mounted on a motorised rotational stage moving at sidereal rate to track the Sun, and transferred it into the lab. As shown in Tab. 1.1, the coherent length of the Sun is about 80 μm, and thus a collection aperture diameter of roughly 1 mm was sufficient, without the use of large telescopes. At the same working wavelength of 546.1 nm, we find $g^{(2)}(0) = 1.3 \pm 0.1$ and a coherence time $\tau_c = 0.26 \pm 0.05$ ns, with $\chi_r^2 = 1.0244$ over an integration time of 45 minutes. The reduction in the visibility of the photon bunching is likely predominantly due to the exponential long-tail component in the APD detector timing response, which we shall attempt to verify in the next chapter.

2.4 Outlook

We have successfully developed and demonstrated an experimental technique to resolve and explicitly measure the temporal photon bunching from thermal blackbody light sources, for both discrete spectrum and blackbody spectrum such as the Sun. We observed a photon bunching signature, i.e., the excess of $g^{(2)}(0)$ above 1, that exceeds the recently reported records of $g^{(2)}(0) = 1.03$ [Karmakar et al., 2012] and $g^{(2)}(0) = 1.04$ [Liu et al., 2014] by about an order of magnitude. These results have been published in [Tan et al., 2014].

Compared to the photon bunching observations using two-photon absorption [Boitier et al., 2009], our method should work at astronomical intensity levels, and not be constrained to cases with the simultaneous arrivals of two photons at the same detector, thus allowing for measurements by detectors and telescopes separated by large baselines.

Using a 14-inch aperture telescope to observe the 80 brightest stars in the night sky, we would expect to collect in the range of 10^4 to 10^5 photoevents/sec within a 2 GHz spectral bandwidth, which translates to a peak $\mathrm{g}^{(2)}(0)$ signal-to-noise ratio of approximately 10 after about an hour of measurement. The integration time should also improve with the use of a time stamp unit without significant dead time as the correlator, rather than an oscilloscope that measures only consecutive two-photoevent coincidences.

Now that we have demonstrated the practical feasibility to resolve and directly observe the temporal correlation behaviour of blackbody radiation, the next chapter shall investigate possible effects by the atmospheric turbulence on timing correlation measurements of stellar light sources such as the Sun. We will also revisit and improve the spectral filtering scheme, so as to reduce the discrepancies observed in the blackbody photon bunching signatures between the Sun and the Argon arc lamp.

Chapter 3

Atmospheric Turbulence

With the measurement scheme illustrated in Fig. 2.1 previously demonstrated for blackbody radiation sources under lab conditions, we now address the atmospheric and weather conditions to investigate possible effects of decoherence on temporal photon bunching measurements of stellar light sources.

Ground-based astronomical observations suffer from atmospheric turbulence [Blazej et al., 2008; Cavazzani et al., 2012; Dravins et al., 1997] that conventionally require adaptive optics and particular geographic conditions to compensate, or orbital platforms to bypass. One of the promises of optical intensity interferometry is its independence from atmospherically induced phase fluctuations [Foellmi, 2009; Hanbury-Brown, 1974]. By performing narrowband spectral filtering on sunlight and conducting temporal intensity interferometry using actively quenched avalanche photon detectors (APDs), the Solar $g^{(2)}(\tau)$ signature can be directly measured [Tan et al., 2014].

We observe a record averaged photon bunching signal of $g^{(2)}(\tau) = 1.693 \pm 0.003$ from the Sun, limited by APD response [Ghioni et al., 2008], consistently throughout the day despite fluctuating weather conditions, cloud cover and elevation angle [Bennett, 1982; Woolf, 1968]. This demonstrates the robustness of the intensity interferometry method against atmospheric turbulence and opto-mechanical instabilities, and the feasibility to implement measurement schemes with both large baselines and long integration times.

3.1 Optical Intensity Interferometry

Hanbury-Brown & Twiss [1954, 1956b] demonstrated that at sufficiently short baselines or timescales, both the spatial and temporal correlation measurements of thermal light sources such as the stars should exhibit a photon bunching signal, which was later generalised by Glauber [1963] as the second order correlation, $g^{(2)}$, that peaks at twice the value of the statistically random noise floor:

$$g^{(2)}(\tau) = 1 + e^{-2|\tau|/\tau_c}, \tag{3.1}$$

where τ_c is the coherence time. This phase-independent characteristic behaviour is the basis for intensity interferometry, which has the benefit of being insensitive to first order noise contribution from urban light pollution and atmospheric turbulence [Davis et al., 1999].

The spatial $g^{(2)}(b)$ imparts information about the shape and intensity distribution of the light source, while the temporal $g^{(2)}(\tau)$ reveals the characteristic emission mechanism of its source, such as whether its a coherent laser light or an incoherent thermal source [Fox, 2006; Loudon, 2000; Mandel & Wolf, 1995; Morgan & Mandel, 1966].

Intensity interferometric measurements thus reveal information about the angular size and path difference of the light source as discussed earlier in Section 1.1, and are so in turn potentially affected by decoherence in the spatial and temporal domains, respectively.

3.1.1 Atmospheric Turbulence

Atmospheric turbulence introduces scintillation with a characteristic timescale on the order of microseconds, and a spatial inner-scale of approximately 3 mm for typical wind speeds of 10 ms^{-1} [Dravins et al., 1997], corresponding to delay time variations on the order of tens of picoseconds due to fluctuations in the atmospheric path difference [Cavazzani et al., 2012; Dravins & LeBohec, 2007].

This sets the lower bound on effective detector timing resolution to be in the 10 ps regime before it is constrained by the atmospheric scintillation, agreeing with the timing uncertainty due to the varying refractive index in the atmospheric layers [Marini & Murray, 1973] as observed in laser ranging experiments [Blazej et al., 2008; Kral et al., 2004].

The Wiener-Khinchin theorem asserts that the auto-correlation function of a stationary random process is given by the Fourier transform of its power spectrum [Khinchin, 1934; Wiener, 1930], which may pick up this timing uncertainty in a $g^{(2)}(\tau)$ photon bunching measurement.

The spatial analogue would be atmospheric seeing, which extends the Airy patterns of stellar light sources into seeing discs, with a typical diameter on the order of arcseconds. The Sun with an angular extension of 0.5° has a coherent length of approximately $80\,\mu$m at 569.6 nm [McKechnie, 2015], according to the van Cittert-Zernike theorem [van Cittert, 1934; Zernicke, 1938] which connects the complex degree of coherence of light at two points with the normalised Fourier transform of the angular intensity distribution of the light source, or by estimates using the Rayleigh Criterion [Fox, 2006]. This spatial complication is more prominent in observing stars other than the Sun, for when the coherent length of the stars are longer than the telescope aperture size; this is further reason why we choose to measure the Sun in this chapter, so as to focus on the temporal characteristics. One way to avoid this problem would be to convert the instruments from fibre-pigtailed into free-space modules.

The atmosphere also induces phase differences of about 0.5 radian between optical light waves with a frequency difference of only a few Gigahertz (GHz) [Dravins et al., 2005], for a corresponding loss of correlation estimated to be less than 1 %. This suggests a practical spectral bandwidth to be in the range of GHz to suppress this chromatic dispersion.

In this chapter, we investigate the possible effects of turbulence in an atmospheric column varying over the time of the day on the temporal photon bunching signature in an intensity correlation measurement of the Sun. The optical bandwidth in our experiment is narrow enough to resolve the emission nature of a light source, with the goal of eventually detecting temporal decoherence effects of non-atmospheric origin.

3.2 Experimental Setup

Similar to the prior chapter, Sunlight is collected by an aspheric lens with an effective focal length of 4.51 mm into a single mode optical fibre for 450 nm to 600 nm (numerical aperture NA = 0.13). The small diameter aspheric lens is sufficient here because the Sun is an angularly extended thermal light source. Thus, the number of photons per spatial mode per unit frequency distribution is defined only by the source surface temperature, and independent of the collection aperture size [Planck, 1900; Stokes, 1994].

The projection into the fundamental TEM_{00} Gaussian mode of the single mode fibre leads to a light field with perfect spatial coherence behind the optical fibre, which is then directed through an arrangement of narrowband spectral filtering as illustrated in Fig. 3.1, replacing the combination of a grating monochromator and a single etalon that we used in our earlier work [Tan et al., 2014], so as to improve the peak transmission and to make the instruments more sturdy mechanically for field transport and operations outside of the controlled laboratory environment, thus enabling this series of Solar $g^{(2)}(\tau)$ measurements to be repeated for 7 days: 27th, 28th Apr and 4th, 5th, 25th, 26th, 28th of May 2015.

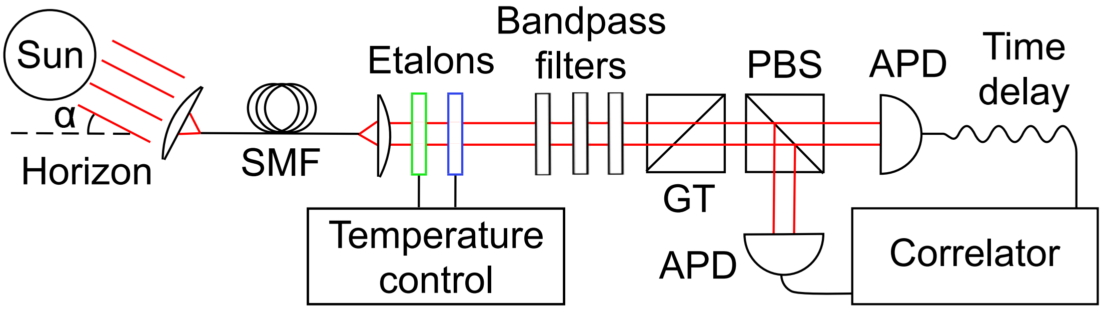

Figure 3.1: Optical setup: Sunlight is coupled into a single mode optical fibre for spatial mode filtering, and exposed to a stack of spectral filters, consisting of two temperature-stabilised etalons E1, E2, and a bandpass filter stack (BPF) of three interference filters. One polarisation of the transmitted narrow spectrum is selected by a Glan-Taylor polariser, and distributed with a polarising beam splitter (PBS) to avalanche photodiodes (APD) for photo-detection time analysis.

3.2.1 Narrowband Etalon Coating

In the filtering scheme employed here, the Sunlight leaving the optical fibre is collimated by an aspheric lens with an effective focal length of 4.6 mm. The light is then sent through two plane-parallel solid etalons of thickness 0.5 mm and 0.3 mm made out of fused silica (Suprasil311). With a refractive index of $n = 1.460$ around 546..570 nm, this corresponds to free spectral ranges

$$FSR = \frac{c}{2dn} \tag{3.2}$$

of approximately 205 GHz and 342 GHz, respectively. The etalons have design reflective coatings on both sides of $R = 97\,\%$ at 546.1 nm as shown in Fig. 3.2.

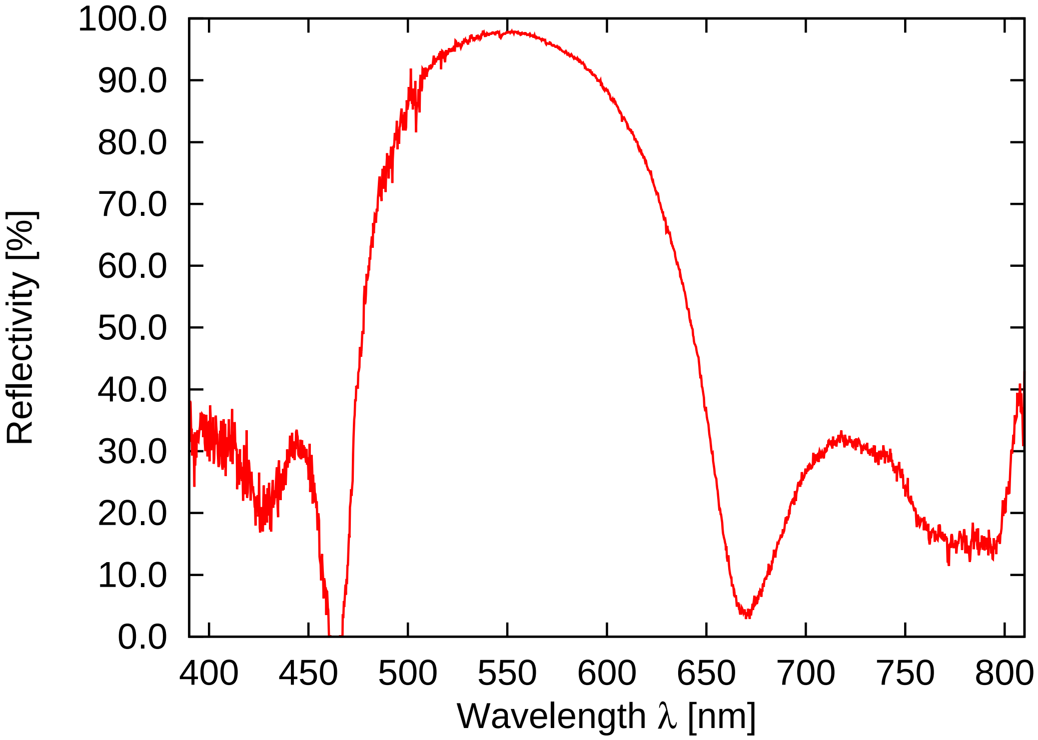

Figure 3.2: The transmission spectrum of this second coating run centred at 546.1 nm, different from the previous broadband coating of 390 nm to 810 nm shown in Fig. 2.4, as measured by a grating monochromator of 0.12 nm resolution. This is to have a variable finesse via choice of wavelength, and to avoid any possible complications due to the previous etalon coating involving over 40 layers.

Neglecting losses in the reflective coatings, the finesse [Fox, 2006]

$$\mathfrak{F}_{\mathfrak{R}} = \frac{\pi\sqrt{R}}{1-R} = 103 \tag{3.3}$$

of the etalons leads to a transmission bandwidth of $\Delta f_{\mathrm{FWHM}} = FSR/\mathfrak{F}_{\mathfrak{R}} = 3.32\,\mathrm{GHz}$ for the 0.3 mm etalon, and $\Delta f_{\mathrm{FWHM}} = 1.99\,\mathrm{GHz}$ for the 0.5 mm etalon, respectively, when centred at the design wavelength of 546.1 nm. At the operating wavelength of 569.6 nm, the reflectivity finesse reduces to approximately 96, corresponding to transmission bandwidths of 3.56 GHz and 2.14 GHz for the 0.3 mm and 0.5 mm etalons respectively.

The spectral transmission profiles of the etalons are tuned via temperature, with a tuning coefficient of $-4.1\,\mathrm{GHz}\,/\mathrm{K}$. Temperature tuning was used in lieu of physical rotation of the etalons to avoid ‘walk-off’ effects [Green, 1980], and for mechanical stability of the setup.

3.2.2 Filter Stack

A series of three interference bandpass filters is used to reject all other wavelengths: two narrowband filters with central wavelength (CWL) of 569.6 nm and Full Width at Half Maximum (FWHM) of 2.2 nm, and a broadband filter with CWL of 540 nm and FWHM of 80 nm. The transmission profile of the bandpass filters (BPF), and the transmission profiles of a combination of the BPF with etalons is shown in Fig. 3.3.

For a single etalon, several transmission peaks corresponding to its free spectral range fall into the transmission window of the BPF. By combining both etalons with their different free spectral ranges, we can achieve single transmission peak in the BPF window, and thus a single transmission window over the whole optical frequency range.

The transmission profiles in Fig. 3.3 for the etalons are wider than actual due to the spectrometer resolution limited at 0.12 nm as observed in Fig. 2.2 (top part). This corresponds to a bandwidth of about 110 GHz, so we are unable to resolve the 0.5 mm etalon’s ideal transmission bandwidth of about 2 GHz (FWHM). Equally, the side lobes next to the transmission peak in Fig. 3.3 are an artefact of

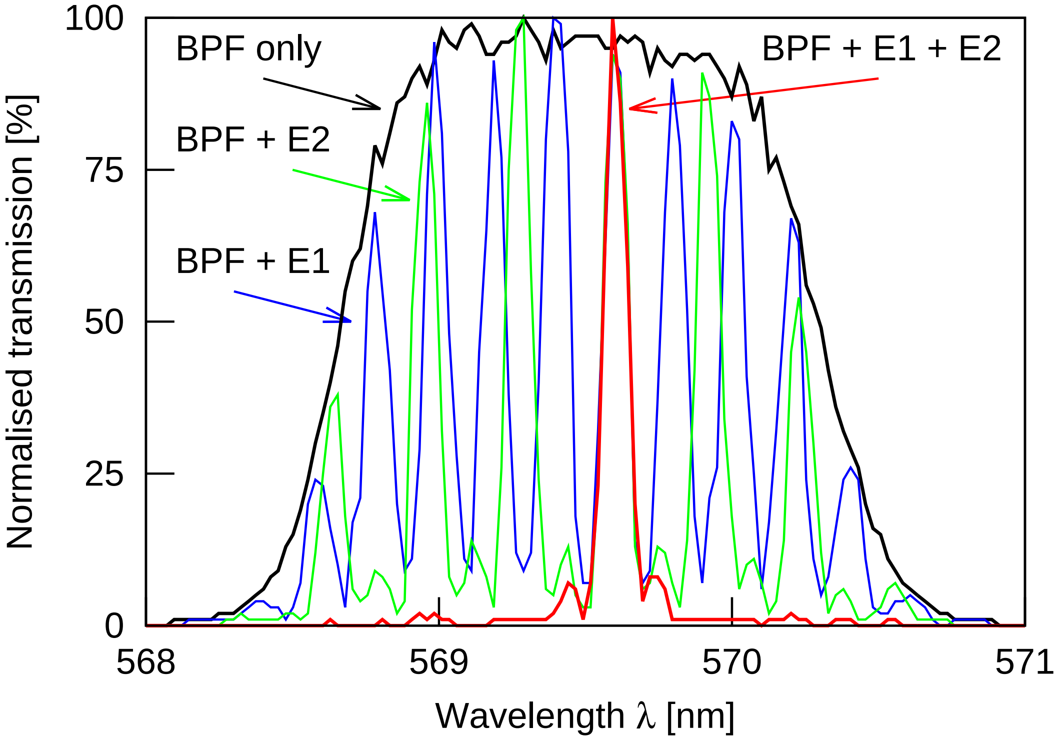

Figure 3.3: Transmission profile of the filter stack. The black trace shows the bandpass filter stack (BPF) only, with a width of 2 nm (FWHM). When adding etalon E1 (thickness 0.5 mm), several transmission peaks fall into the window selected by the BPF. Similarly, wider spaced transmission peaks are visible with etalon E2 (thickness 0.3 mm). When combining both etalons and the BPF, only one transmission peak is left, with small residual contributions about 0.6 nm due to near-overlaps. The linewidth of the transmission peaks with the etalons is dominated by the spectrometer response of 0.12 nm, the actual line width should be around 0.002 nm.

the spectrometer we used. We estimate the peak transmission of the etalon and filter stack to be around 84%, improving the transmission of the grating/etalon stack in the previous chapter by about a factor of 4.

The strong emission line at 569.6 nm in Gamma Velorum (γ^2 Vel), which is the brightest Wolf-Rayet star at visual apparent magnitude $m_v = 1.7$, is a prime natural laser source candidate [Dravins & Germanà, 2008], and would be an interesting astrophysical light source to apply this photon correlation method to. Therefore, this wavelength was chosen as an instrumental proof-of-concept.

To centre the peak transmission of the etalon stack at 569.6 nm, we filtered the blackbody spectrum of an Argon arc lamp with a grating monochromator to a bandwidth of about 0.12 nm. With this, we could align the bandpass interference filters, and tune the etalon temperatures. The 0.5 mm etalon had to be maintained at 59.2°C, and the 0.3 mm etalon at 64.0°C.

3.2.3 Detector Response

A Glan-Taylor (GT) polariser selects linearly polarised light to optimise spatial mode correlations and in conjunction with a polarising beamsplitter (PBS), allows for the balancing of detector count rates, thus minimising the measurement duration. This configuration also helps to suppress cross-talk coincidence events arising from the APD breakdown flash [Kurtsiefer et al., 2001].

Finally the light is detected by two actively quenched Silicon Avalanche Photon Detectors (APDs). An oscilloscope with a sampling rate of 40 GS/s was used to determine the temporal correlation $g^{(2)}(\tau)$. The combined effective timing jitter of photodetectors and oscilloscope was measured to be around $\tau_j = 40\,\mathrm{ps}$ (FWHM) as shown in Fig. 2.3, but the joint timing response of the two photodetectors has a peculiar structure as illustrated in Fig. 3.4 and agrees with the instrument response function provided by manufacturer in Fig. 2.5. The coincidence distribution of the detectors shows a narrow central peak leading to the small full width at half maximum, but a relatively large base that seems to reflect an exponential decay. The solid lines in the figure represents a heuristic model:

$$G^{(2)}(\tau) = A\frac{1}{\sqrt{2\pi\sigma^2}}e^{-\tau^2/2\sigma^2} + B\frac{2}{\tau_e}e^{-|\tau|/\tau_e}\,, \tag{3.4}$$

with a time constant $\sigma = 12.0 \pm 0.1\,\mathrm{ps}$ for the Gaussian, and $\tau_e = 225 \pm 1\,\mathrm{ps}$ for the exponential decay for a fit over the time window $\tau = -1\ldots1\,\mathrm{ns}$. The statistical weights A and B of the two distributions are about the same.

It is significant that the contribution from the central Gaussian peak structure with $\sigma = 12.0 \pm 0.1\,\mathrm{ps}$, is similar in magnitude with the contribution by the exponential tail structure with time constant $\tau_e = 225 \pm 1\,\mathrm{ps}$. This suggests that the conventional consideration, of the detector timing jitter τ_j to be the timing

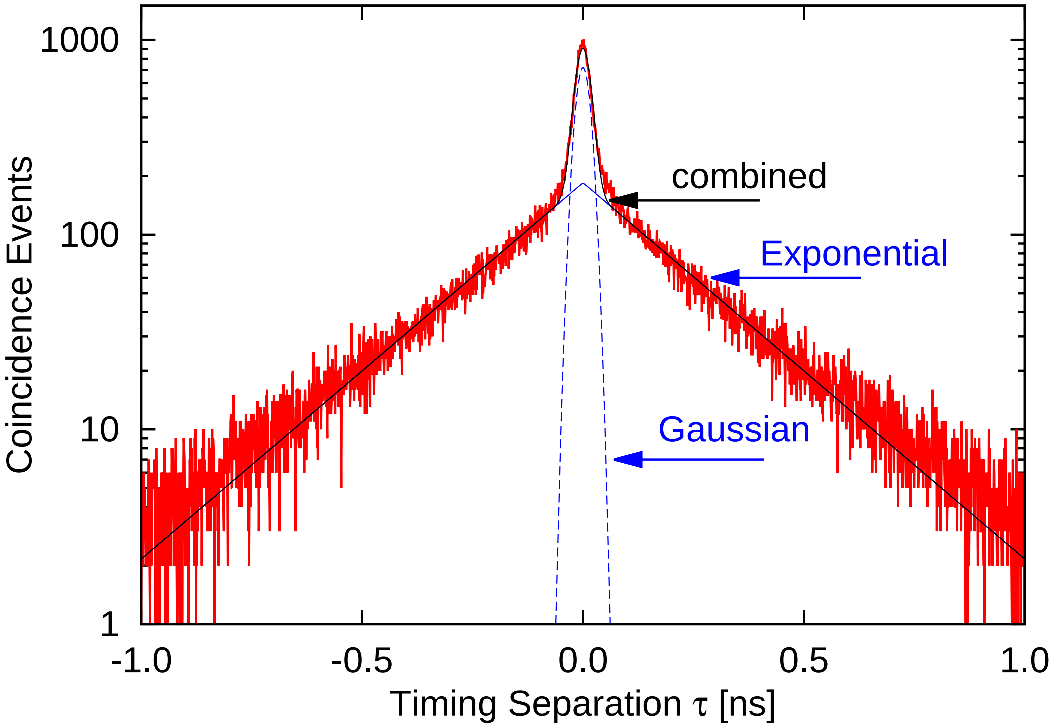

Figure 3.4: Photodetection coincidence histogram from photon pairs at $\lambda = 810\,\mathrm{nm}$ generated by parametric down conversion with very short intrinsic timing spread. This coincidence histogram reveals information about the timing uncertainty introduced by the detection mechanism only, dominated by APD timing jitter. The dominant central structure can be fitted to a Gaussian, with the long tails following an exponential decay, as modelled in Eqn. 3.4.

response FWHM, is not accurate because about half of the photoevents are in the exponential tail component.

We currently lack a precise model of the photodetector timing behaviour, although Ghioni et al. [2008] suggests that some photon detectors have an internal cavity to increase the quantum efficiency by enhancing the optical field inside the detector at resonant wavelengths, but would extend the timing response with a longer diffusion tail as a consequence. The peculiar detector response is most likely the dominant contribution that is limiting the maximally observed photon bunching signature (of roughly 1.7) from the ideal blackbody characteristic peak value of $g^{(2)}(0) = 2$, and might be improved by using photon detectors without the internal cavity.

3.3 Results

These measurements were conducted in the National University of Singapore observatory site, with geographical coordinates of $1°17'49''$ N and $103°46'44''$ E, on the 28th of May 2015, from 11:36 am to 5:36 pm (GMT +8:00), through varying cloud cover, weather conditions and elevation angular position of the Sun.

A single typical 4-minute $g^{(2)}(\tau)$ measurement of the Sun is shown in Fig. 3.5. The two-photon coincidence events are fitted to a Lorentzian due to the etalons defining the transmitted frequency distribution. The fitted parameters give a peak $g^{(2)}(\tau = 0)$ value of 1.69 ± 0.05 corresponding to an interferometric visibility V $\approx 83\%$ and a coherence time of $\tau_c = 370 \pm 35$ ps.

In Fig. 3.6, the Solar $g^{(2)}(\tau = 0)$ is measured in 4-minute time intervals over the afternoon of 28 May 2015. The corresponding elevation angle α of the Sun given by

$$\sin(\alpha - R) = \sin\phi \sin\delta + \cos\phi \cos\delta \cos\omega \tag{3.5}$$

as shown in the top part of the figure, with latitude ϕ, declination δ and hour angle ω [Woolf, 1968] and a small heuristic correction R of at most 34 arcminutes due to the refraction in the atmosphere [Bennett, 1982].

Over that measurement time where weather and building geometry permitted to collect data, the elevation angle α covers a range from about 70° around noon to 20° in the evening, making the length of the air column

$$s = h_0/\sin\alpha \tag{3.6}$$

that the light has to pass through to range from $1.06h_0$ to $2.92h_0$, where h_0 is the effective height of the atmosphere. Within the statistical uncertainty, we do not discern any distinct change of the peak correlation $g^{(2)}(\tau = 0)$.

As reference, to investigate decoherence effects contributed by the atmospheric turbulence, we compare the Solar $g^{(2)}(\tau = 0)$ measurements with that of an Argon arc lamp having a blackbody temperature of 6000 K and thus a suitable analogue to the Sun. Both the Sun and the lamp deliver $\approx 10^5$ photoevents per second to the photon detectors after the filtering scheme, which lends further confidence to the arc lamp as a fair analogue to the Sun.

The mean Solar $g^{(2)}(0) = 1.693 \pm 0.003$ is significantly higher than our previous value of 1.37 ± 0.03 as discussed in chapter 2, though still slightly lower than the 1.8 estimated from the convolution $\tilde{g}^{(2)}(\tau)$ of the etalon response of $\tau_c = 370\,\text{ps}$:

$$\tilde{g}^{(2)}(\tau) = g^{(2)}(\tau) \otimes L(\tau) = \int g^{(2)}(\tau - \tau')L(\tau')d\tau' \,, \tag{3.7}$$

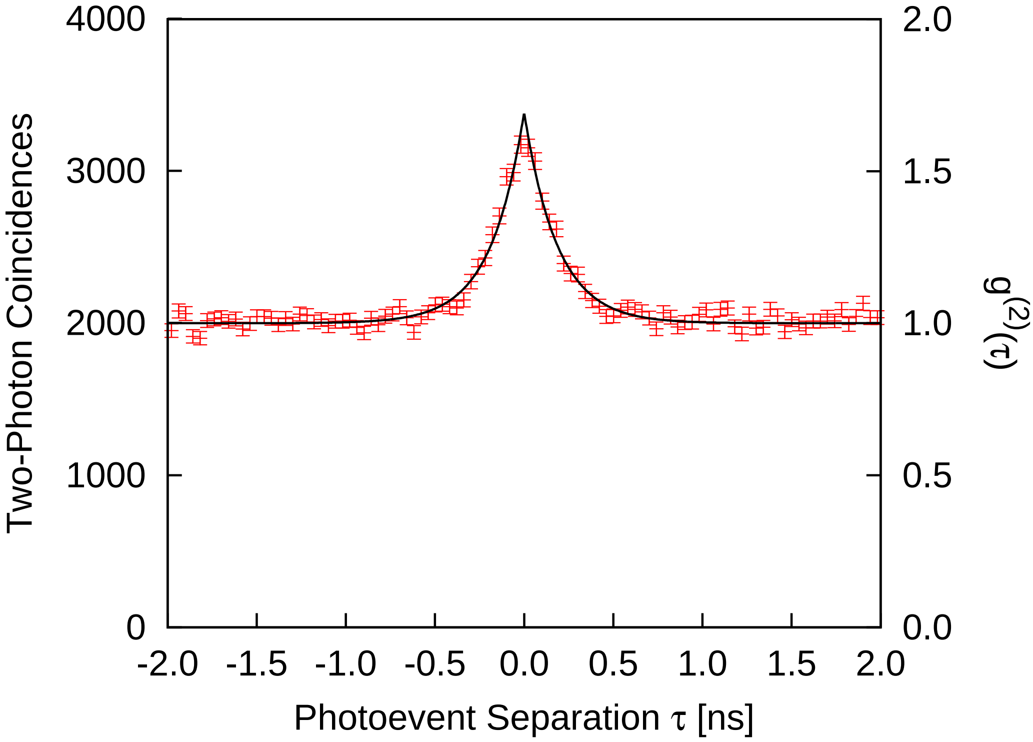

Figure 3.5: Raw coincidence histogram and normalised intensity correlation function $g^{(2)}(\tau)$ for the Sun, measured in a 4-minute interval, starting at 11:36 am. The characteristic photon bunching signature decays exponentially with a time constant of $\tau_c = 370 \pm 35\,\text{ps}$ from the maximum $g^{(2)}(0) = 1.69 \pm 0.05$.

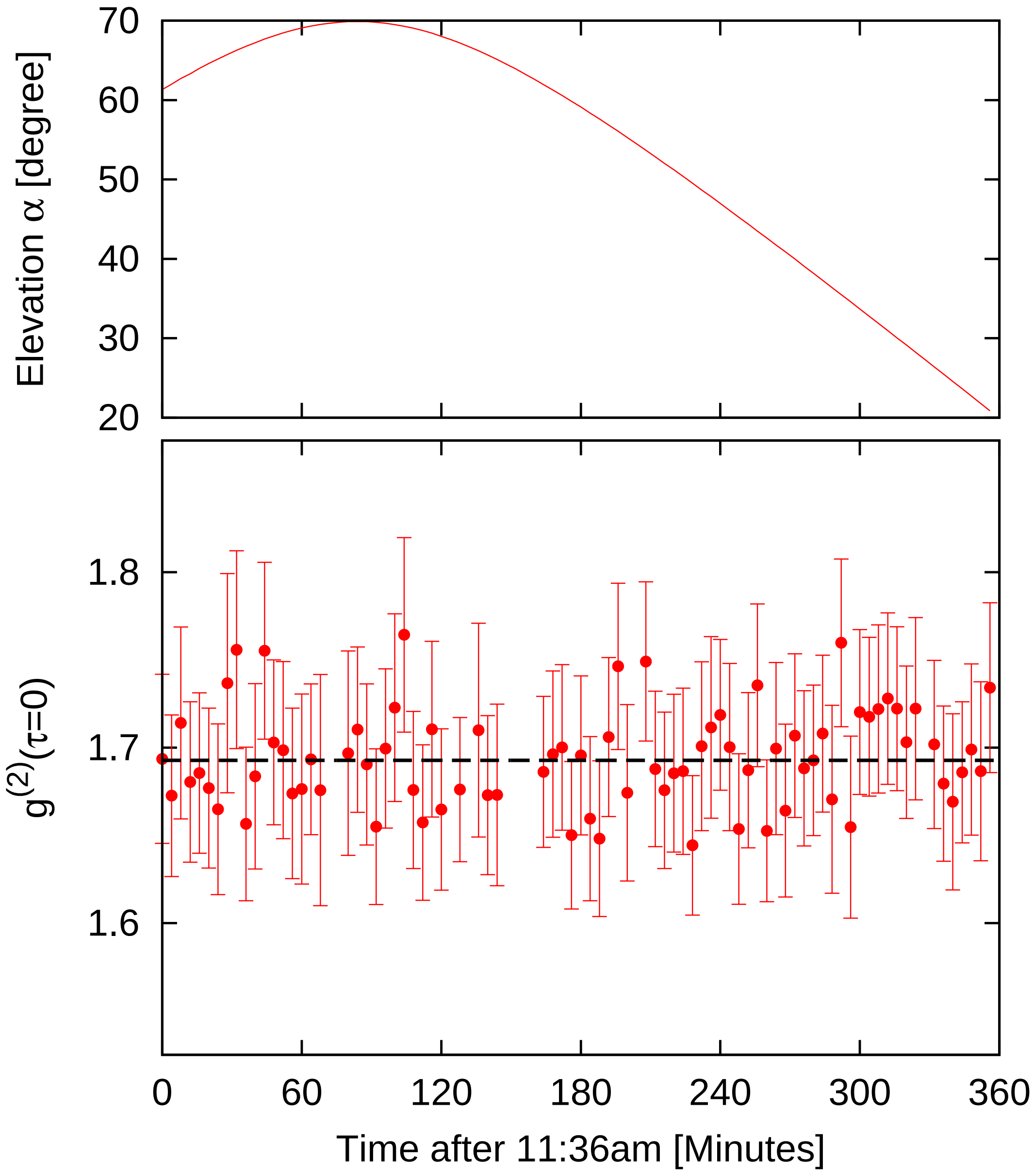

Figure 3.6: Bottom trace: Normalised peak correlation $g^{(2)}(0)$ of the Sun, taken in 4-minute intervals over an extended duration from 11:36 am onwards, with some gaps in the trace when it was too cloudy to collect sufficient light within 4 minutes to produce a significant measurement. The black dotted line shows the averaged Solar $g^{(2)}(0) = 1.693 \pm 0.003$. Top trace: the corresponding elevation α of the Sun.

with an APD timing jitter $\tau_j = 40\,\mathrm{ps}$ (FWHM) following a Lorentz distribution

$$L(\tau) = \frac{1}{\pi}\frac{\tau_j/2}{\tau_j^2/4 + \tau^2}\,. \tag{3.8}$$

This discrepancy may be attributed to minor temperature gradient due to uneven heating in the etalons leading to slightly different transmission spectrum across the input beam profile. There could also be a difference in the etalon linewidth due to it operating away from the etalon design wavelength of 546.1 nm, or a deviation of the photodetector response function $L(\tau)$ from a Lorentzian. We did not use the broadband etalons here due to the lack of 0.3 mm substrates in that batch, which we need in order for the filter stacking to have a larger effective free spectral range FSR, i.e. lowest common multiple of two etalon FSR values.

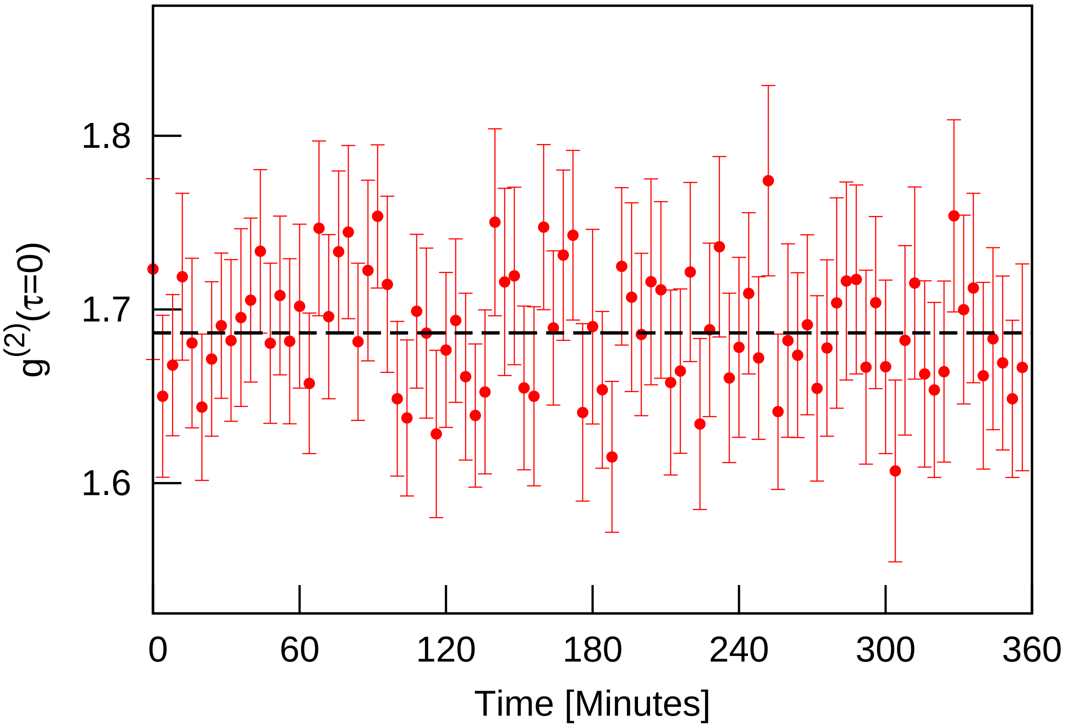

Figure 3.7: Normalised peak correlation $g^{(2)}(0)$ of an Argon arc lamp in intervals of 4 minutes for testing the thermal/temporal stability of the optical setup and as a control reference for the Solar measurements through the atmosphere.

However, if we perform a convolution between the heuristic $G^{(2)}(\tau)$ model (Eqn. 3.4) for the detector response fitted in Fig. 3.4, with an ideal etalon response with $\tau_c = 500\,\mathrm{ps}$ corresponding to $\Delta f_{FWHM} = 2\,\mathrm{GHz}$, the resulting peak $g^{(2)}\tau = 0) = 1.63$, which is slightly lower than the averaged measurement of Solar $g^{(2)}\tau = 0) = 1.693 \pm 0.003$ as indicated in Fig. 3.5. This suggests that the exponential component of the detector timing response is significant, and thus insufficient to simply equate a detector timing jitter τ_j with the FWHM of the timing response.

The Solar $g^{(2)}(\tau = 0) = 1.693 \pm 0.003$ is also compatible within statistical uncertainty with the average Argon arc lamp $g^{(2)}(\tau = 0) = 1.687 \pm 0.004$ as shown in Fig. 3.7, which serves as a control source of blackbody radiation.

3.4 Outlook

The agreement within statistical uncertainty of the temporal photon bunching measurements between the Sun and the control Argon arc lamp suggests that the atmospheric turbulence and variable weather conditions do not degrade the measurable visibility of timing correlation measurements, under our instrumentation scheme of 2 GHz optical bandwidth and 25 GHz electronic bandwidth.

Furthermore, the Solar $g^2(\tau)$ photon bunching measurements remain consistent over half a day of measurements, during which the Solar elevation position covered about 50° of angular travel across the sky. This demonstrates the robustness of temporal correlation measurements against different depths of air column in which the measured light passes through, and thus suggests this technique to be applicable in observing other stellar light sources. These results have been published in [Tan et al., 2016]

The next chapter will subject the instrumentation to blackbody radiation mixed with different laser light contributions, so as to test the capabilities of the measurement scheme in identifying light sources that deviate from the characteristic blackbody behaviour.

Chapter 4

Identifying Laser Light within Blackbody Radiation

The previous chapters have shown that the temporal intensity interferometry technique (Section 2.1), when performed with narrowband spectral filtering and fast avalanche photon detectors, allows for probing the temporal correlation behaviour of blackbody radiation sources, including observations of the Sun through the atmosphere without degrading the measurable visibility. This chapter will evaluate the capabilities of the measurement scheme to identify laser light contributions of various intensities from within a blackbody radiation spectrum.

4.1 Blackbody Sources with Laser Light

Stellar objects emitting both blackbody radiation and stimulated spectral line emissions, or lasers, have been discovered in astronomy in the non-optical bands. Natural optical lasers, however, have thus far remained unverified, although they have been suspected to be present in energetic stars like η Car and Wolf-Rayet stars including γ^2 Vel, but their predicted spectral linewidths are too narrow to directly resolve for confirmation tests against predicted values [Dravins & Germanà, 2008].

Astrophysical Non-Optical Lasers

Natural non-optical lasers from astrophysical sources were speculated [Menzel, 1970; Varshni & Nasser, 1986] soon after the detection of strong interstellar microwave emissions from molecular gas clouds [Weaver et al., 1965], following the successful amplification of both microwave and optical wavelengths in laboratory experiments. Planetary infrared lasing emissions were also identified in the upper atmospheres of Venus and Mars [Taylor, 1983]. Water masers have been subsequently detected from comet halos as well [Hofner & Churchwell, 1996].

Stellar infrared laser emissions were detected from MWC 349, a double star system in the constellation Cygnus by the NASA Kuiper Airborne Observatory [Strelnitski et al., 1995]. This natural infrared lasing line at 169 μm is caused by the intense stellar ultraviolet radiation pumping the circumstellar disk of high-density hydrogen gas which serve as the gain medium, with an output intensity over six times higher than the non-amplified spontaneous emissions at this wavelength [Thum et al., 1995].

Astrophysical Optical Lasers

Natural optical laser light from astrophysical sources remain pending confirmation, with a prime candidate being the highly energetic η Car stellar system that was once the second brightest star in the night sky, 2300 parsecs away from Earth, where 1 parsec (pc) is the distance of an object such that one astronomical unit (roughly the orbital radius of the Earth) subtends one arcsecond, which translate to approximately 3.26 light-years, or 3.1×10^{16} m.

It is also the only known stellar source of ultraviolet laser radiation [Davidson et al., 1995, 1997], and potentially producing optical laser light as well [Johansson & Letokhov, 2005], pending observational confirmation. With predicted linewidths between 30 MHz to 100 MHz, these optical spectral lines cannot be resolved by existing astronomical spectrographs as yet [Griest et al., 2010].

4.1.1 Coherent Laser Light

The theoretical framework for stimulated emissions was formulated by Einstein [1916], which was further elaborated by Schawlow & Townes [1958] who proposed the practical amplification of electromagnetic radiation by stimulated emission, creating the first maser (Microwave Amplification by the Stimulated Emission of Radiation). Later Maiman [1960] developed the first laser (Light Amplification by Stimulated Emission of Radiation). For laser amplification to take place, the thermal non-equilibrium condition of population inversion is required, normally by energy being pumped from an external power source into the gain medium [Fox, 2006].

Consider then an ideal laser, as a perfectly coherent light beam with constant angular frequency ω, phase ϕ and amplitude $\mathcal{E}_0$, as described by $\mathcal{E}(x,t) = \mathcal{E}_0 \sin(kx - \omega t + \phi)$. Such a laser light source would appear quasi-monochromatic with relatively high intensity, but is insufficient to be characterised by these degrees of freedom alone.

Instead, an additional constraint to characterise laser light would be by its temporal correlation properties. Coherent laser light obeys Poissonian statistics which, being a random distribution, has a time-independent intensity I_0 and thus a constant second order correlation $g^{(2)}$ [Foellmi, 2009; Hanbury-Brown, 1974] such that

$$g^{(2)}(\tau) = \frac{\langle I(t)I(t+\tau)\rangle}{\langle I(t)\rangle^2} = \frac{I_0^2}{I_0^2} = 1\,. \tag{4.1}$$

In contrast, the second order correlation [Fox, 2006] for blackbody radiation can be described by

$$g^{(2)}(\tau) = 1 + e^{-2|\tau|/\tau_c}\,, \tag{4.2}$$

as seen earlier to exhibit a temporal photon bunching behaviour within a characteristic timescale τ_c [Hanbury-Brown & Twiss, 1954, 1956b; Morgan & Mandel, 1966].

4.2 Experimental Setup

In order to test whether the temporal intensity interferometry technique developed in this thesis could help to identify blackbody objects with optical laser emissions, a test light source is simulated by taking joint contributions from a laser light source with a blackbody radiation source, and then performing timing correlation measurements.

We use a laser source (Osram PL520 50mW diode) that generates an emission line at 513.8 nm, under laboratory room temperature of 25.7 °C, at an operating current of 66.4 mA. When the laser diode operates below the lasing threshold current measured to be about 59 mA, it becomes a light emitting diode (LED) instead with broadband spectrum and a thermal photon bunching signature.

A blackbody radiation source via an Argon arc lamp functions as the in-lab analogue to a regular star, with an effective blackbody temperature of 6000 K,

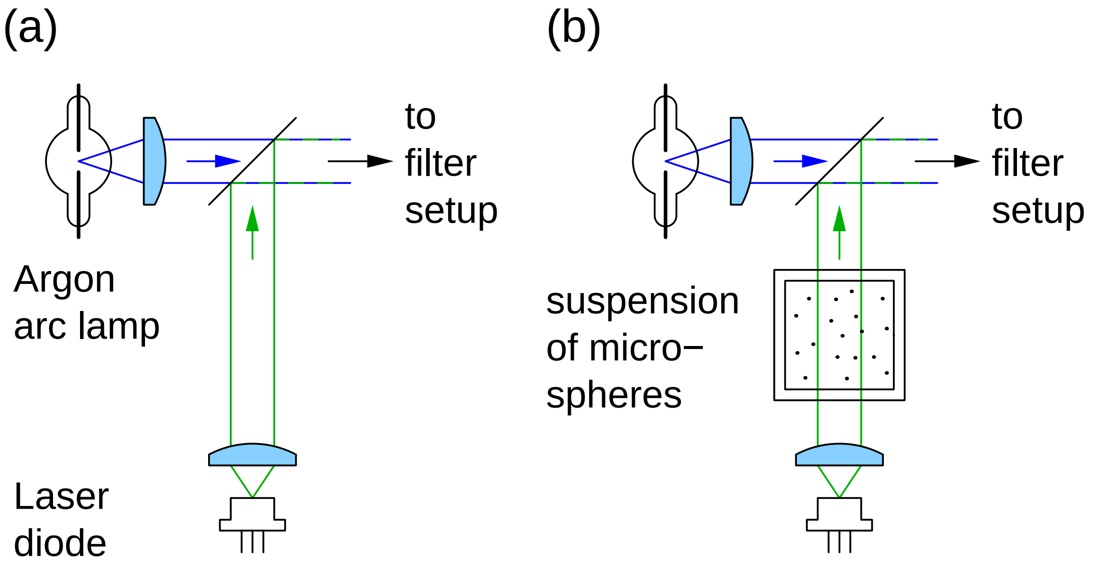

Figure 4.1: (a) A test light source with the coherent 513.8 nm laser light partially reflected from a microscope glass slide, mixed with the transmitted blackbody radiation contribution from the Argon arc lamp. (b) A second test light source where the 513.8 nm laser light is sent through a suspension of 0.2 μm microspheres, which serve as scattering centres, to induce Doppler broadening in the laser light, before mixing with the blackbody radiation contribution from the Argon arc lamp.

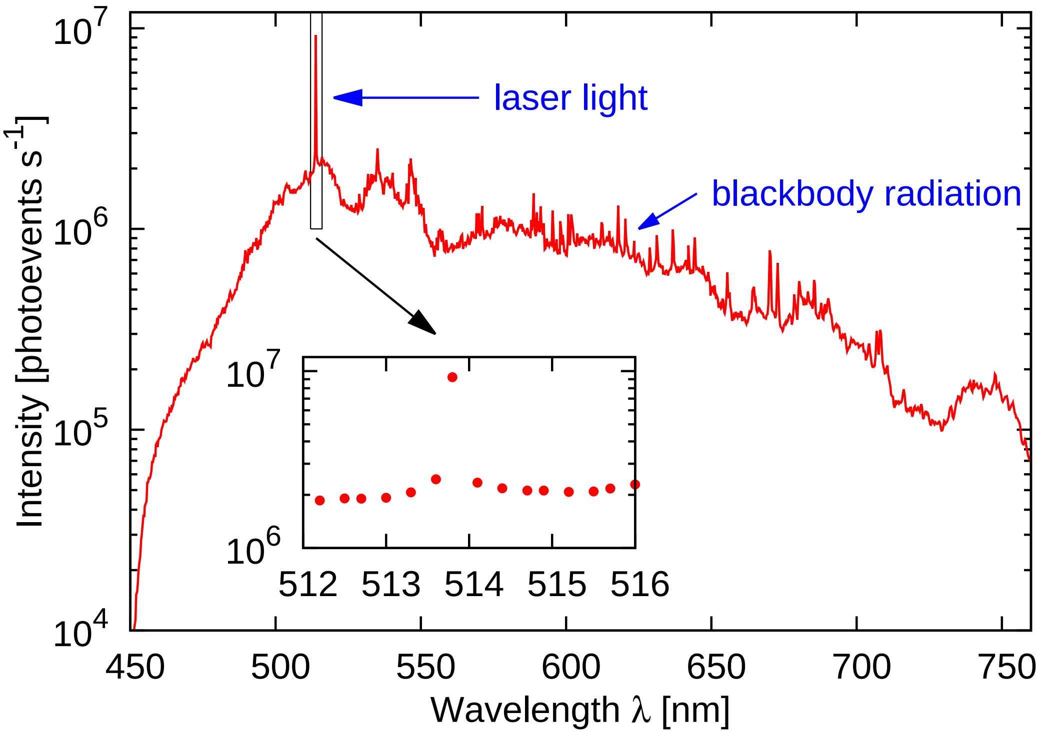

Figure 4.2: Spectrum of the test light source in Fig. 4.1, obtained by coupling a combination of coherent green laser light at 513.8 nm with blackbody radiation from Argon arc lamp of effective temperature $T = 6000\,\mathrm{K}$ into a single mode optical fibre.

which is comparable to the surface temperature of the Sun and of similar spectrum with the Sun as seen earlier in Fig. 2.7.

These two light contributions are combined using a piece of microscope glass slide, without anti-reflective coatings, as a simple asymmetric non-polarising beamsplitter as shown in Fig. 4.1(a), coupling approximately 4 % of the incident laser light with 92 % of the Argon arc lamp output. The resultant spectrum is shown in Fig. 4.2, measured by the grating monochromator illustrated in Fig. 2.2 (top part) with approximately 0.12 nm resolution.

A second test light source is configured with a Doppler broadened laser light at 513.8 nm, as shown in Fig. 4.1(b), by sending the coherent laser light through a cubic plastic cuvette at normal incidence, containing water with a suspension of standard mono-disperse polystyrene microspheres which are 0.1 % solids [weight/volume] in water, of 0.2 μm diameter [Dravins et al., 2015]. These microspheres serve as scattering centres with Brownian motion due to thermalisation from the room temperature, with the resultant speckling and phase randomisation causing the laser light to exhibit photon bunching behaviour [Arecchi, 1965; Hard et al., 1977; Martienssen & Spiller, 1964; Scarl, 1966, 1968], with a characteristic linewidth that is the FWHM of the Fourier transform of the $g^{(2)}(\tau)$ second order correlation measurement. The resultant intensity of the Doppler broadened laser light is too low, relative to the blackbody radiation contribution, to feature and be identified in a spectral measurement.

The coherence properties of the laser light caused by the suspension is dependent on the temperature of the suspension, the viscosity (ratio of water to microspheres), and beam focus [Dravins & Lagadec, 2014]; these parameters were not fully characterised, and we instead settled through a number of trials for this particular setting as sufficient for our test objective to have a Doppler broadened laser light. In lieu of the expensive microspheres, other liquid suspension have been tried during the course of the experiment, including milk, which yield surprisingly similar effects for much lower costs. This is likely due to the fat globules in the beverages serving as the scattering centres, from the industrial process of homogenisation of the milk.

To identify the laser light from the blackbody radiation in these two test light sources, the narrowband filtering scheme shown in Fig. 4.3 is centred at 513.8 nm. The instruments have an effective resolving power in the regime of $R = 2 \times 10^5$, which is comparable to current astronomical spectrographs [Griest et al., 2010].

In the filtering scheme, the light from the test sources is coupled into a single mode fibre in order to enforce spatial coherence for maximal interferometric visibility and filter performance. The light is then collimated through a grating monochromator, which has a reflective diffraction grating blazed at 500 nm, with 1200 lines/mm. The monochromator is calibrated at normal incidence to the 546.1 nm line in a Hg discharge lamp, with a transmission FWHM of 0.12 nm. With the grating at $-1.175\,^\circ$ orientation, the filtered light at this alignment is centred at 513.8 nm to identify the laser light contribution.

The light is then sent through a pair of plane-parallel solid etalons made of fused silica (Suprasil311), with reflectivity coatings of R = 97 % and thus an

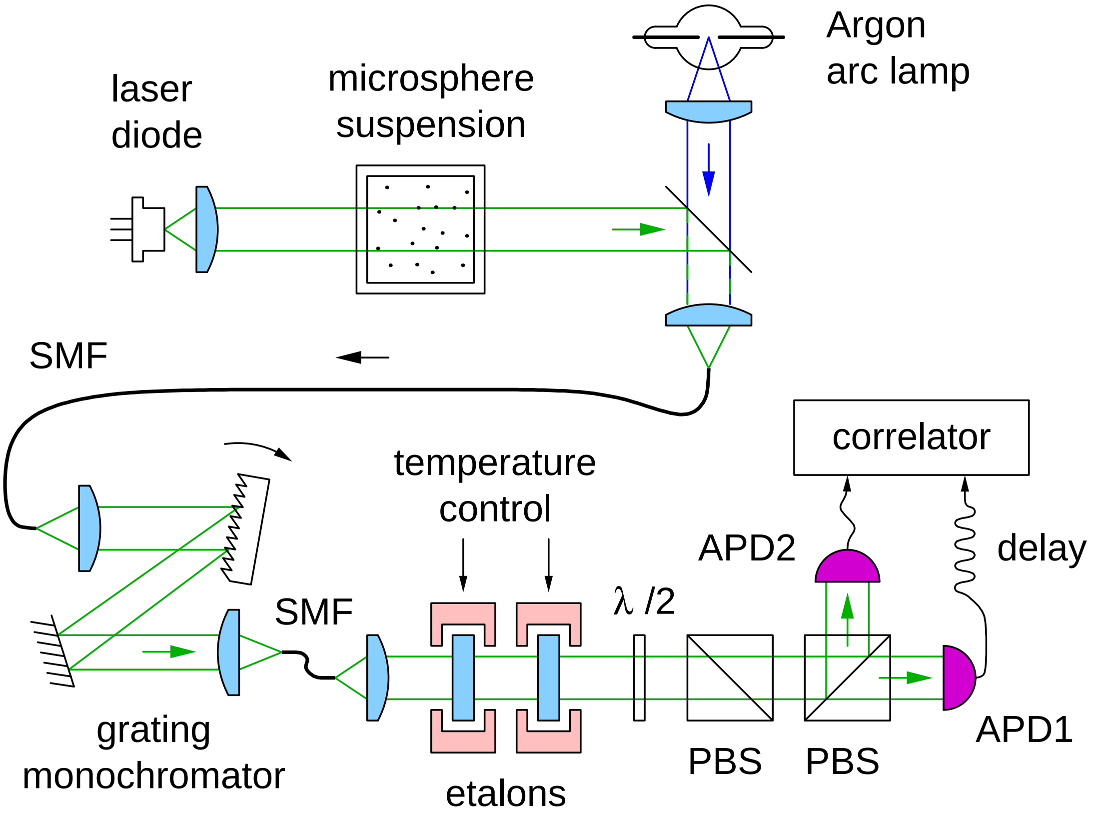

Figure 4.3: Setup to filter and identify the 513.8 laser light from the blackbody radiation spectrum provided by the Argon arc lamp. The filtered mix of laser light and blackbody radiation is received by a pair of photon detectors to measure their timing correlations.

ideal reflectivity finesse of $\mathcal{F}_{\mathfrak{R}} = 103$. The etalons have thicknesses of 0.5 mm and 0.3 mm, with their temperatures stabilised at 48 °C and 77 °C, respectively. This stacking of etalons, in conjunction with the diffraction grating earlier in the filtering sequence, suppresses the majority of the thermal blackbody background, transmitting only a bandwidth of 2 GHz as seen in Fig. 3.3.

However, if this experimental scheme is to be deployed for measuring stars, the grating monochromator should be replaced with a high-transmission (≈ 99 %) bandpass filter with FWHM ≈ 2 nm, similar to the filtering used earlier in Fig. 3.1. This is due to the poor transmission of the grating monochromator at 15 %. The grating monochromator is used here, due to resource limitations at the time to obtain such a bandpass filter centred at 513.8 nm.

The filtered light is sent through a beamsplitter, then into a pair of actively quenched silicon avalanche photon detectors, where coincidence photoevents are measured using a digital oscilloscope, with an effective timing jitter τ_j of 40 ps. The photon detectors have a relatively low dark count rate of 50 photoevents/sec, predominantly from the detector thermal noise (dark counts) rather than ambient light, and is effectively negligible in the subsequent coincidence measurements.

Timing correlation measurements of the test light sources are measured for four different mixing ratios of laser light with blackbody radiation. In all the mixing ratios, the blackbody radiation contribution from the Argon arc lamp is on the order of 10^4 photoevents/sec, and between 3×10^4 to 6×10^6 photoevents/sec from the laser light source.

4.3 Results

Coherent Laser Light within Blackbody Radiation

As demonstrated in the (laser:weak) plot in Fig. 4.4, when the coherent laser contribution is comparable in intensity ($\approx 10^4$ photoevents/sec) with the blackbody background contribution after narrowband 2 GHz spectral filtering, the presence of a coherent laser source may be revealed by a reduction in the temporal photon bunching signal, relative to the (laser:absent) measurement in Fig. 4.4 with the

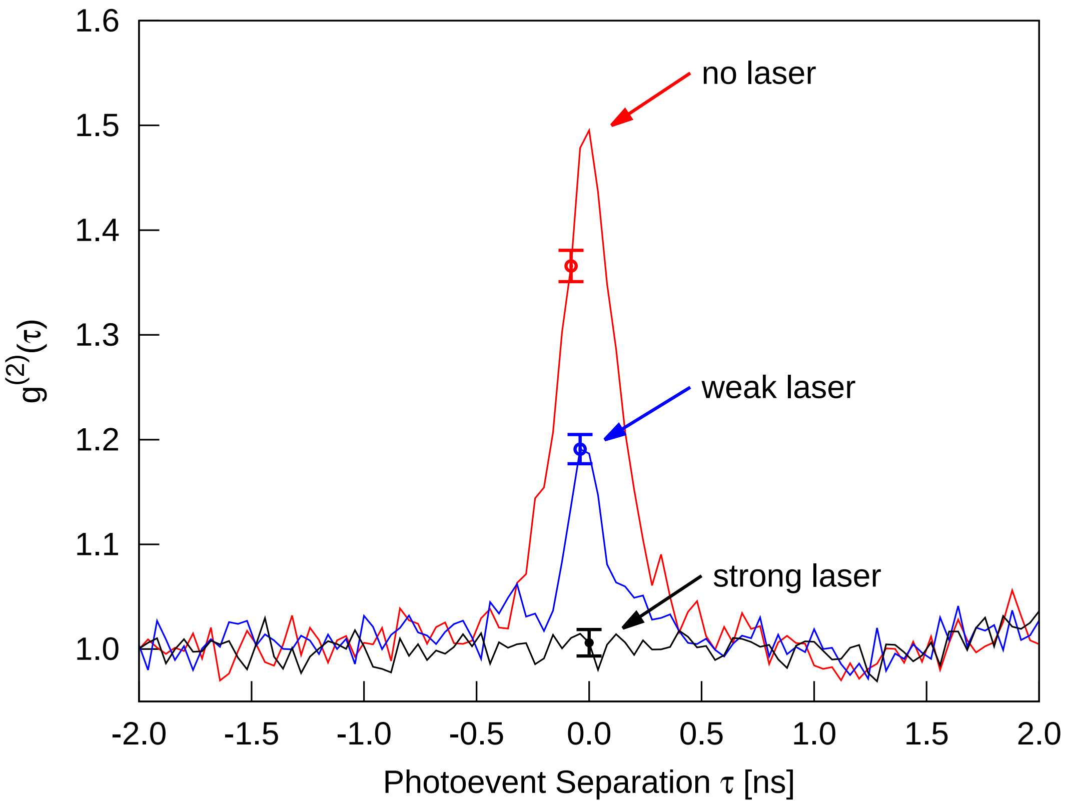

Figure 4.4: Temporal photon bunching measurements for different mixing ratios: consistent intensity of incoherent thermal light from the Argon arc lamp at approximately 3×10^4 photoevents/sec, but mixed with various contribution levels of the coherent laser light. Where (laser:strong) has 6×10^6 photoevents/sec of laser light, (laser:weak) has 3×10^4 photoevents/sec, and (laser:absent) has none. The measurements all accumulated 10^6 coincidence photoevents, to allow for easier direct comparisons of the resulting histograms.

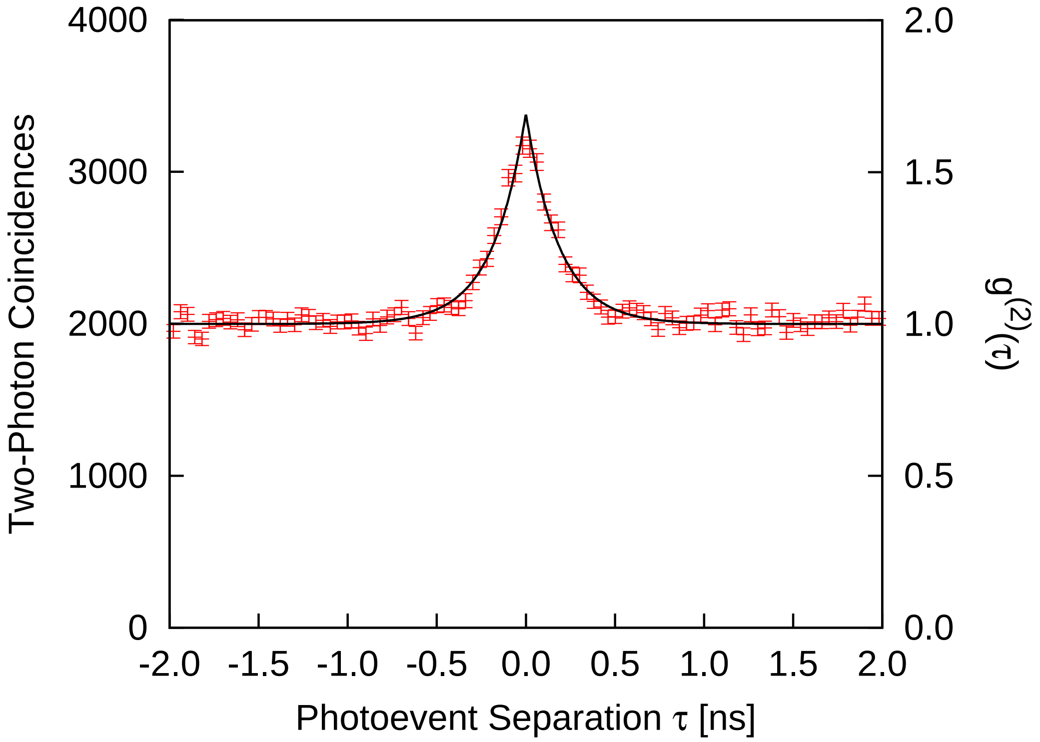

A reproduction of Fig. 3.5 shown here for clarity.

detector-limited blackbody temporal bunching signature of approximately 1.7 as observed earlier in Fig. 3.5 as well.

When the intensity of the coherent laser emission is significantly higher than the blackbody background, as in the (laser:strong) results shown in Fig. 4.4 where the laser light contribution is over 2 orders of magnitude in intensity than the filtered blackbody contribution, similar to the spectrum illustrated in Fig. 4.2, the timing correlation measurements appear constant and flat within statistical uncertainty without an observable excess bunching signature from the blackbody contribution. This is due to the random correlations of the coherent laser light statistically dominating the two-photoevent coincidence measurements.

Doppler Broadened Laser Light within Blackbody Radiation

Using the second test light source in Fig. 4.1 with the Doppler broadened 513.8 nm laser light mixed with the blackbody radiation contribution from the Argon arc lamp, we observe the timing correlation histogram illustrated in Fig. 4.5, which shows a wider bunching signal due to the Doppler broadened laser light with $g^{(2)}(0) = 1.227 \pm 0.005$ and a coherence time $\tau_c = 44 \pm 2\,\text{ns}$, corresponding to a linewidth of approximately 23 MHz, which is comparable to literature estimates

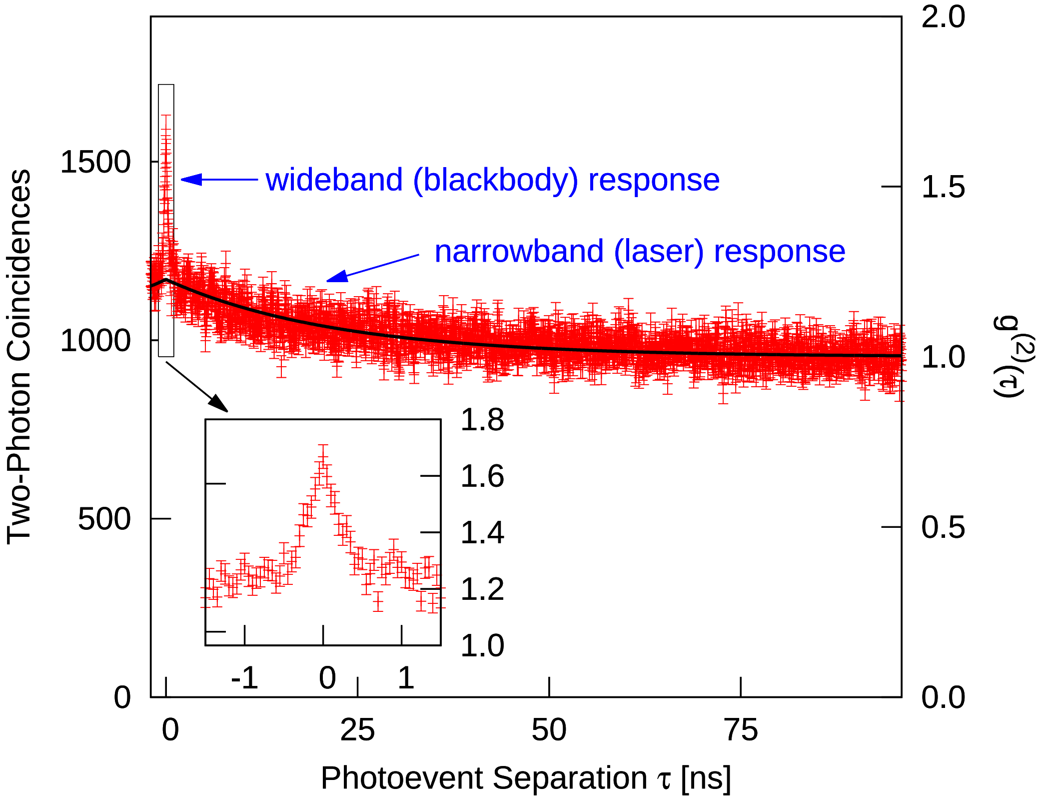

Figure 4.5: Measurements of two-photoevent coincidences from the mixing of filtered blackbody radiation from an Argon arc lamp (wideband response) with Doppler broadened laser light contribution at 513.8 nm (narrowband response), both at similar rates around 2×10^4 photoevents per second. The measurements collected a total of 2×10^6 coincidence events, to accommodate reduced laser light intensity after Doppler broadening.

for natural laser linewidths [Dravins & Germanà, 2008].

The narrowband response with the broader $g^{(2)}(0)$ peak of 1.227 suggests a $\sqrt{0.227} \approx 47.6\%$ contribution by the Doppler broadened laser light. This implies a $(52.4\%)^2 \approx 0.274$ contribution by the blackbody radiation from the Argon arc lamp which gives the narrow photon bunching signal in the wideband response.

4.4 Outlook

The narrowband spectral filtering instrumentation was able to identify the presence of laser light that is mixed with blackbody radiation, by suppressing the blackbody contribution and performing timing correlation measurements of the laser light with the filtered blackbody radiation. The coherent laser light contributions could be identified by the reduction in the temporal photon bunching signal, compared against a reference bunching signature from a blackbody radiation source without laser light contributions. This might be achieved by tuning the etalon transmission, so as to perform $g^{(2)}(\tau)$ measurements across a spectrum, and identifying wavelengths with reduced bunching values as compared with their spectral neighbourhood, similar to Fig. 4.4.

The measurement scheme was also able to determine the linewidth of Doppler broadened laser light within a blackbody spectrum, by measuring the timing correlations of both the blackbody radiation and the laser light, beyond the wavelength resolution capabilities of astro-spectrographs [Griest et al., 2010].

These results suggest that the measurement technique presented may be suitable to assess the temporal coherence properties of light sources that deviate from blackbody behaviour due to an additional laser light contribution.

Chapter 5

Summary and Outlook

Stellar intensity interferometry is a remarkable combination of quantum optics and astronomy with some compelling advantages and results [Hanbury-Brown, 1974], but did not receive widespread adoption [Davis et al., 1999]. This technique has thus far been considered mainly for the evaluation of the spatial coherence properties of stars to infer their stellar angular diameters [van Cittert, 1934; Zernicke, 1938], but seemed to have limited room for development due to the low signal-to-noise ratio. After a brief review in Section 1.1 of the spatial coherence interferometry in the early Hanbury-Brown and Twiss experiments, we considered in Section 1.2 the limitations of the signal-to-noise and the assumption of stars as approximations to ideal blackbody radiation sources.

In the main body of this work, we explored options to carry out temporal correlation measurements, by probing the coherence timescales of blackbody light sources such as stars with their characteristic spectral distribution [Planck, 1900], and thus circumvent the limitations by the signal-to-noise ratio in spatial correlations [Hanbury-Brown, 1974].

The Sun was probed as a near-ideal blackbody radiation source to demonstrate the practicality of temporal correlation measurements of blackbody light sources [Tan et al., 2014]. This was done by using a Fabry-Pérot solid etalon as a main filter, with a blazed diffraction grating as a pre-filter to perform narrowband spectral filtering to $\Delta\nu_{FWHM} \approx 2\,\mathrm{GHz}$, and a pair of actively quenched avalanche photon detectors having a combined timing jitter of $\tau_j = 40\,\mathrm{ps}$ to obtain the two-photoevent coincidence histograms.

The instrumentation allowed us to observe the temporal photon bunching signatures for three different types of thermal light sources: a Mercury discharge lamp with a discrete spectrum, an Argon arc lamp with a continuous spectrum at an effective blackbody temperature of $T = 6000\,\mathrm{K}$, and the Sun as a natural blackbody approximation. Integrating over 45 minutes at $\lambda = 546.1\,\mathrm{nm}$, the preliminary measurements for the Sun resulted in a bunching signal of $g^{(2)}(0) = 1.3 \pm 0.1$ with a corresponding coherence time of $\tau_c = 0.26 \pm 0.05\,\mathrm{ns}$. The bunching signal can be modelled as a Lorentzian as defined by the etalon response, with $\chi_r^2 = 1.0244$. The Solar photon bunching signature, although resolved, was lower than both the measured values for the Argon arc lamp with $g^{(2)}(0) = 1.45 \pm 0.03$ and a shorter coherence time $\tau_c = 0.31 \pm 0.01\,\mathrm{ns}$ with a reduced $\chi_r^2 = 1.066$, as well as for the Mercury discharge lamp with $g^{(2)}(\tau = 0) = 1.79 \pm 0.01$ and an exponential decay with a characteristic coherence time of $\tau_c = 0.436 \pm 0.006\,\mathrm{ns}$.

Nevertheless, the measured temporal photon bunching signature, i.e., the excess of $g^{(2)}(0)$ above 1, exceeds the recently reported records of $g^{(2)}(0) = 1.03$ [Karmakar et al., 2012] and $g^{(2)}(0) = 1.04$ [Liu et al., 2014] by about an order of magnitude. This indicates that with narrowband spectral filtering, it is possible to significantly increase the coherence timescale of blackbody radiation sufficiently for modern actively quenched photon detectors to resolve the temporal photon bunching signal of blackbody radiators such as the Sun and other stars.

We modified the spectral filtering scheme by removing the grating monochromator as a first-stage spectral filter, and used a stacking of two etalons with slightly different thicknesses instead to increase the effective free spectral range, matched to a stack of three interference bandpass filters. The improved filtering scheme with its stronger suppression of the blackbody spectrum increased the measured Solar $g^{(2)}(\tau = 0) = 1.693 \pm 0.003$, which is significantly higher than our previous record, and is compatible within statistical uncertainty with the Argon arc lamp $g^{(2)}(\tau = 0) = 1.687 \pm 0.004$ used as a control source of blackbody radiation.

The improved scheme also increased transmission efficiency, which reduced the integration time for Solar $g^{(2)}$ measurements from 45 minutes previously to 4 minutes, and thus allowed us to probe for possible temporal decoherence effects by the varying atmospheric air column depths [Bennett, 1982; Marini & Murray, 1973] through measuring the Solar temporal correlations in angular steps of 1°.

The instruments were then exposed to four different preparations and mixing ratios of blackbody radiation generated by the Argon arc lamp, combined with a laser light source at 513.8 nm, corresponding to different astrophysical scenarios. We observe that when mixed with a blackbody background by the Argon arc lamp, it is possible to find a laser emission line from the continuous blackbody spectrum and suppress the blackbody contribution sufficiently, in order to identify the temporal correlation properties of the laser light.

Specifically, by suppressing the blackbody spectral contribution from a continuous spectrum down to only $\approx 2\,\mathrm{GHz}$ and a reduced intensity of about 3×10^4 photoevents/sec, the instruments were able to identify a coherent laser signal within the blackbody spectrum. The measurement scheme could distinguish between the absence of laser light which gave a photon bunching signature similar to Fig. 3.5, the presence of a relatively weak coherent laser signal of 3×10^4 photoevents/sec which gave a reduced bunching signal, and a relatively stronger coherent laser signal of 6×10^6 photoevents/sec with which the Poissonian statistics dominated resulting in a flat histogram.

The instruments were further tested with a laser light contribution at 513.8 nm, but that has been Doppler broadened by microspheres of $0.2\,\mu$m diameter which serve as scattering centres [Dravins et al., 2015], suspended in room temperature water undergoing Brownian motion. The instrumentation scheme allowed to determine the coherence time of the broadened laser signal to be $\tau_c = 22 \pm 1\,\mathrm{ns}$, corresponding to a linewidth of approximately 45 MHz and with $g^{(2)}(0) = 1.227 \pm 0.005$, which is similar to the predicted linewidth values for natural lasers [Dravins & Germanà, 2008].

Outlook

We propose some astrophysical scenarios in which the temporal correlation measurement scheme developed in this thesis may be useful, through the use of narrowband spectral filtering and fast photon detectors.

Natural Optical Laser

There are some energetic stellar systems such as η Car and Wolf-Rayet stars like γ^2 Vel that have been observed to emit not just blackbody radiation, but also narrowband optical emission lines estimated to be on the order of tens of MHz [Dravins & Germanà, 2008; Johansson & Letokhov, 2005; Roche et al., 2012; Strelnitski et al., 1995], which are beyond modern astronomical spectrographs to resolve [Griest et al., 2010; Tellis & Marcy, 2015]. These emission lines could be caused by natural optical lasing mechanisms, with the star providing the pump source of energy, and outer shell of stellar materials/clouds serving as the lasing medium [Castor & Nussbaumer, 1972; van der Hucht, 2001].

We propose using narrowband spectral filtering to isolate one of these stellar emission lines, and suppress the blackbody contribution, so as to increase the signal-to-noise ratio of the discrete-line signal over the stellar blackbody contribution, and to verify its timing correlation behaviour.

Optical SETI

Shortly after lasers were discovered, there began a concurrent movement by Drake [1961] to search the 21 cm band in the radio spectrum for potential extraterrestrial intelligence (SETI), with a call led by Dyson [1960] to extend the search into the infrared wavelength regime. Schwartz & Townes [1961], who had just invented the masers and lasers in the laboratories, initiated Optical SETI, which was later picked up by Sagan & Drake [1975] and recently in July 2015 by Stephen Hawking [Merali, 2015]. The Optical SETI programme scans for optical laser signals [Forgan, 2014; Korpela et al., 2011; Merali, 2015; Townes, 1983]. Such an optical laser signal will be spatially unresolved with its host star, and thus difficult to isolate from the stellar blackbody spectrum and identify the coherent laser signature.

In the scenario when there is a coherent laser light signal, but with low intensity, the laser signal may not be apparent nor distinct from the blackbody contribution of its host star. As demonstrated in the (laser:weak) plot of Fig. 4.4, when the coherent laser contribution is comparable in intensity ($\approx 10^4$ photoevents/sec) with the blackbody background contribution after narrowband (2 GHz) spectral filtering, the presence of a coherent laser source may be revealed by a reduction in the temporal photon bunching signal. Therefore, a timing correlations measurement sweep across the spectrum may allow for the locating and identification of such a low intensity but coherent laser signal from a stellar blackbody background.

‘True’ Randomness

A source of ‘true’ randomness, or random number generator, would have fundamental implications such as in Bell’s Inequality tests [Gallicchio et al., 2014], as well as technological relevance in quantum cryptography and quantum key distribution [Li et al., 2015] for security applications, or perhaps even generate game outcomes for casinos.

Such a source might be derived by measuring the correlations between two causally disconnected stellar light sources [Pimbblet & Bulmer, 2004], i.e. stars beyond their mutual light cones, such that at the moment of correlation measurement on Earth, the two stellar sources would not have had enough time to ‘communicate’ with each other, barring the existence of a local hidden variable, and thus produce ‘true’ uncorrelated light.

Quantum Gravity

Some theories of quantum gravity suggest the possible discretisation of space-time, but such a space-time foam structure [Perlman et al., 2015] would be far too small to detect directly, being on the order of Planckian scale [Milburn, 1991, 2006]. However, light that have propagated over cosmic distances and timescales might accumulate sufficient temporal decoherence, to an extent that may be measurable [Lieu & Hillman, 2003; Maziashvili, 2009; Ng et al., 2003].

The instrumentation developed in this thesis is unlikely to have reached the necessary precision nor sensitivity to probe for such temporal decoherence, where any effects should be just a modest deviation from the photon bunching signature with $g^{(2)}(\tau = 0) = 2$ of an ideal blackbody radiation source, but is perhaps a promising tool for further development towards this goal.

Beyond the traditional application of estimating the angular size of a celestial object via its spatial coherence length, this technique may also be used to measure photon decoherence of starlight across extended time-scales and distances, which are impossible to create in Earth-based laboratory conditions. Such experiments may provide complementary observational evidence that help to set constraints in theoretical models of quantum gravity [Lieu & Hillman, 2003; Maziashvili, 2009; Ng et al., 2003; Ragazzoni et al., 2003]. These potential astrophysical applications would be discussed in the concluding Chapter 5.

Optical Pulsar Clock

Radio pulsars have been used as a precise time standard, which is essential to the accurate determination of spatial positions and trajectories on Earth, a task which can be accomplished by atomic clocks and the Global Positioning System (GPS) network of satellites [Matsakis & Foster, 1995]. Although an ‘unhackable’ source of timing reference has particular value for security applications, the length scale of radio wavelengths requires the instrumentation to be correspondingly bulky and generally immobile.

Thus we propose the development in photon-timing correlation measurements of millisecond optical pulsars, such as the Crab Pulsar with an apparent magnitude of 16.5 and approximately 30 Hz repetition, with the goal of making the telescope and electronics portable.

Multi-Spectral Bands

As we have seen earlier in Eqn. 1.21, the signal-to-noise ratio (SNR) of stellar intensity interferometry is independent of the optical bandpass, in the regime where the detector are unable to resolve the coherent timescale of the light source.

Therefore, the SNR of stellar intensity interferometry could be increased by introducing a pair of Echelle gratings to diffract the input starlight into a two-dimensional projection of the spectrum. This spectrum could then be imaged onto an array of photon detectors, for simultaneous temporal correlation measurements [Dravins & Lagadec, 2014; Ofir & Ribak, 2006a,b].

Appendix

Journal Publications

The core results from Chapters 2 and 3 are respectively published in:

Measuring Temporal Photon Bunching in Blackbody Radiation, P. K. Tan, G. H. Yeo, H. S. Poh, A. H. Chan and C. Kurtsiefer, The Astrophysical Journal Letters, Vol. 789, L10 (2014), and

Optical Intensity Interferometry through Atmospheric Turbulence, P. K. Tan, A. H. Chan and C. Kurtsiefer, Monthly Notices of the Royal Astronomical Society, Vol. 457, 4291-4295 (2016).

The manuscript for Chapter 4 is in the process of documentation for arXiv preprint and journal submission.

Scientific Conferences

These are the posters, along with both the contributed and invited talks, that have been presented in scientific conferences regarding this thesis and research.

Event	Location	Date	Contribution
JSPS 7th HOPE Meeting	Tokyo, Japan	Mar 2015	Talk+Poster
Graduate Symposium	NUS, Singapore	Aug 2014	Talk
HBT Workshop	Nice Observatory, France	May 2014	Talk
Institute of Physics Meeting	NUS, Singapore	Feb 2014	Invited Talk
HBT Winter School	Asiago Observatory, Italy	Feb 2013	Talk
IAU 28th General Assembly	Beijing, China	Aug 2012	Poster
NASA Exoplanet Workshop	Caltech, USA	Jul 2012	Poster

Public Talks

These are the invited talks given for general education and public outreach.

Event	Location	Date
Science Bites	Science Centre, Singapore	Nov 2015
IPS Astronomy Retreat	Port Dickson, Malaysia	Jun 2015
Nurturing Leonardos	ArtScience Museum, Singapore	May 2015
Problem Based Learning Symposium	Republic Polytechnic, Singapore	Mar 2015
Visualising the Universe	ArtScience Museum, Singapore	Sep 2014
IPS Astronomy Retreat	Bintan, Indonesia	Jun 2013

References

Allen, C. W. 2000, Allen's Astrophysical Quantities (Springer), editor: Arthur N. Cox xiii, xviii, 1, 2, 10, 13

Arecchi, F. T. 1965, Phys. Rev. Lett., **15**, 912 13, 56

Asakura, T. 1970, Opto-electronics, **2**, 115 13

Barbieri, C., Daniel, M. K., de Wit, W. J., et al. 2009, Astro2010: The Astronomy and Astrophysics Decadal Survey, **2010** iv

Bennett, G. G. 1982, Journal of Navigation, **35**, 255 v, 37, 46, 64

Blazej, J., Prochazka, I., & Kral, L. 2008, Proc. SPIE, **7152**, 71520R v, 4, 37, 39

Boitier, F., Godard, A., Rosencher, E., & Fabre, C. 2009, Nat. Phys., **5**, 267 15, 36

Capraro, I., Naletto, G., Barbieri, C., et al. 2009, in Proceedings of Science: Quantum of Quasars workshop iv

Castor, J. I., & Nussbaumer, H. 1972, MNRAS, **155**, 293 66

Cavazzani, S., Ortolani, S., & Barbieri, C. 2012, MNRAS, **419**, 2349 v, 4, 37, 38

Davidson, K., Ebbets, D., Weigelt, G., et al. 1995, AJ, **109**, 1784 52

Davidson, K., Ebbets, D., Johansson, S., et al. 1997, AJ, **113**, 335 52

Davis, J., Tango, W. J., Booth, A. J., et al. 1999, MNRAS, **303**, 773 iv, 1, 12, 13, 38, 63

Drake, F. D. 1961, Physics Today, **14**, 140 vi, 66

Dravins, D., & Germanà, C. 2008, in The Universe At Sub-Second Timescales, ed. D. Phelan, O. Ryan, & A. Shearer (USA: AIP), 284 vi, xiii, 10, 43, 51, 62, 65, 66

Dravins, D., Jensen, H., LeBohec, S., & Nuñez, P. D. 2010, Proc. SPIE, **7734**, 77340A 9

Dravins, D., & Lagadec, T. 2014, Proc. SPIE, **9146** iv, vi, 56, 69

Dravins, D., Lagadec, T., & Nunẽz, P. D. 2015, Nat. Commun., **6**, 6852 iv, vi, 56, 65

Dravins, D., & LeBohec, S. 2007, Proc. SPIE, **6986**, 698609 iv, 38

Dravins, D., Lindegren, L., Mezey, E., & Young, A. T. 1997, Publications of the Astronomical Society of the Pacific, **109**, 173 v, 13, 37, 38

Dravins, D., Barbieri, C., Deppo, V. D., et al. 2005, QuantEYE: Quantum Optics Instrumentation for Astronomy, Tech. rep., European Southern Observatory OWL Instrument Concept Study 39

Dyson, F. J. 1960, Science, **131**, 1667 vi, 66

Einstein, A. 1916, Deutsche Physikalische Gesellschaft, **18**, 318 53

Estes, L. E., Narducci, L. M., & Tuft, R. A. 1971, J. Opt. Soc. Am., **61**, 1301 13

Fastie, W. G. 1952, JOSA, **42**, 641 22

Foellmi, C. 2009, A&A, **507**, 1719 iv, 8, 9, 12, 37, 53

Forgan, D. H. 2014, Journal of the British Interplanetary Society, **67**, 232 vi, 66

Fox, M. 2006, Quantum Optics: An Introduction (UK: Oxford University Press) 1, 2, 4, 10, 12, 14, 38, 39, 42, 53

Gallicchio, J., Friedman, A. S., & Kaiser, D. I. 2014, Phys. Rev. Lett., **112**, 110405 67

Ghioni, M., Armellini, G., Maccagnani, P., et al. 2008, Photonics Technology Letters, IEEE, **20**, 413 v, 28, 37, 45

Ghosh, G. 1997, Appl. Opt., **36**, 1540 17, 24

Glauber, R. 1963, Phys. Rev., **131**, 2766 iv, 4, 13, 14, 15, 38

Gonsiorowski, T., & Dainty, J. C. 1983, J. Opt. Soc. Am., **73**, 234 13

Green, J. M. 1980, J. Phys. E: Sci. Instrum., **13**, 1302 19, 24, 42

Griest, K., Whitmore, J. B., Wolfe, A. M., et al. 2010, ApJ, **708**, 158 vi, 52, 56, 62, 66

Hanbury-Brown, R. 1974, The Intensity Interferometer: Its Application To Astronomy (London ; New York: Taylor & Francis ; Halsted Press), 184 iv, 6, 8, 12, 13, 37, 53, 63

Hanbury-Brown, R., Davis, J., & Allen, L. R. 1974, MNRAS, **167**, 121 iv, 1

Hanbury-Brown, R., & Twiss, R. Q. 1954, Phil. Mag., **45**, 663 iv, 1, 13, 38, 53

—. 1956a, Nature, **177**, 27 12

—. 1956b, Nature, **178**, 1046 iv, 38, 53

—. 1957, Proc. Roy. Soc., **A242**, 300 iv, 1, 2, 12

—. 1958, Proc. Roy. Soc., **243**, 291 iv, 1, 2, 12

Hard, R., Zeh, R., & Allen, R. D. 1977, J. Cell Sci, **23**, 335 56

Harwalkar, V., Bohidar, H., & Chopra, S. 1983, Appl. Phys. B, **31**, 215 13

Hecht, E., & Zajac, A. 1997, Optics (Addison Wesley) 21

Heraeus. 2013, Quartz Glass for Optics Data and Properties, Tech. rep., Heraeus Quarzglas Gmbh 17

Hofner, P., & Churchwell, E. 1996, A&AS, **120**, 283 52

Hong, C. K., Ou, Z. Y., & Mandel, L. 1987, Phys. Rev. Lett., **59**, 2044 20

Horton, A. J., & Bland-Hawthorn, J. 2007, Optics Express, **15**, 1443 23

Jensen, H., Dravins, D., LeBohec, S., & Nunẽz, P. D. 2010, Proc. SPIE, **7734**, 77341T iv

Johansson, S., & Letokhov, V. S. 2005, New Astronomy, **10**, 361 vi, 52, 66

Karmakar, S., Meyers, R., & Shih, Y. 2012, Proc. SPIE, **8518**, 851805 v, 15, 35, 64

Khinchin, A. 1934, Mathematische Annalen, **109**, 604 39

Korpela, E. J., Anderson, D. P., Bankay, R., et al. 2011, Proc. SPIE, **8152**, 815212 vi, 66

Kral, L., Prochazka, I., Blazej, J., & Hamal, K. 2004, Proc. SPIE, **5240**, doi:10.1117/12.511203 39

Kurtsiefer, C., Zarda, P., Mayer, S., & Weinfurter, H. 2001, J. Mod. Opt., **48(13)**, 2039 20, 44

Labeyrie, A., Lipson, S. G., & Nisenson, P. 2006, An Introduction to Optical Stellar Interferometry (Cambridge University Press) 1, 3, 4, 5

LeBohec, S., Barbieri, C., de Wit, W.-J., et al. 2008, Proc. SPIE, **7013**, 70132E iv

LeBohec, S., Adams, B., Bond, I., et al. 2010, Proc. SPIE, **7734**, 77341D iv

Lecroy. 2011, WaveRunner 6 Zi Oscilloscopes, Tech. rep., Teledyne Lecroy, Inc 20

Li, H.-W., Yin, Z.-Q., Wang, S., et al. 2015, Scientific Reports, **5**, 16200 67

Lieu, R., & Hillman, L. W. 2003, ApJ, **585**, L77 68

Liu, X.-F., Chen, X.-H., Yao, X.-R., et al. 2014, Opt. Letters, **39**, 2314 v, 15, 36, 64

Loudon, R. 2000, The Quantum Theory of Light (Oxford Science Publications) 2, 19, 38

Maiman, T. H. 1960, Nature, **187**, 493 53

Mandel, L., & Wolf, E. 1995, Optical Coherence and Quantum Optics (Cambridge University Press) 2, 4, 11, 14, 38

Marini, J. W., & Murray, C. W. 1973, Correction of laser range tracking data for atmospheric refraction at elevations above 10 degrees, Report X-591-73-35, NASA v, 39, 64

Martienssen, W., & Spiller, E. 1964, Am. J. Phys, **32**, 919 13, 56

Matsakis, D. N., & Foster, R. S. 1995, Amazing Light: Application of Millisecond Pulsar Timing to the Long-Term Stability of Clock Ensembles (Springer-Verlag Press) 68

Maziashvili, M. 2009, Astroparticle Physics, **31**, 344 68

McKechnie, T. S. 2015, General Theory of Light Propagation and Imaging Through the Atmosphere (Springer International Publishing), doi:10.1007/978-3-319-18209-4 39

Menzel, D. H. 1970, in Proceedings of IAU Colloquia No.2 Commission 36, Vol. 332, Spectrum Formation in Stars with Steady-State Extended Atmospheres, ed. H. G. Groth & P. Wellmann, IAU, 134 52

Merali, Z. 2015, Nature, **523**, 392 vi, 66

Milburn, G. J. 1991, Phys. Rev A, **44**, 5401 67

—. 2006, New J. Phys., **8**, 96 67

Millour, F. 2008, New Astronomy Reviews, **52**, 177 13

Morgan, B. L., & Mandel, L. 1966, Phys. Rev. Lett., **16**, 1012 13, 38, 53

Ng, Y. J., Christiansen, W. A., & van Dam, H. 2003, ApJ, **591**, L87 68

Ofir, A., & Ribak, E. N. 2006a, MNRAS, **368**, 1646 69

—. 2006b, MNRAS, **386**, 1651 69

Park, S., Ko, H., & Park, M.-H. 2005, Optical Engineering, **44(4)**, 048001 19

Perlman, E. S., Rappaport, S. A., Christiansen, W. A., et al. 2015, ApJ, **805**, 1 67

Pimbblet, K. A., & Bulmer, M. 2004, Publications of the Astronomical Society of Australia, **22**, 1 67

Planck, M. 1900, Verhandlungen der Deutschen Physikalischen Gesellschaft, **2**, 237 9, 14, 40, 63

Ragazzoni, R., Turatto, M., & Gaessler, W. 2003, ApJ, **587**, L1 68

Rayleigh. 1879, Philosophical Magazine, **8**, 261 5

Roche, P. F., Colling, M. D., & Barlow, M. J. 2012, MNRAS, **427**, 581 vi, 66

Sagan, C., & Drake, F. D. 1975, Scientific American, **232**, 80 vi, 66

Saleh, B. E. A., & Teich, M. C. 2007, Fundamentals of Photonics (John Wiley & Sons) 14

Sansonetti, C. J., & Veza, D. 2010, J. Phys. B: At. Mol. Opt. Phys., **43**, 205003 xiv, 18

Scarl, D. B. 1966, Phys. Rev. Lett., **17**, 663 56

—. 1968, Phys. Rev., **175**, 1661, issue 5 14, 56

Schawlow, A. L., & Townes, C. H. 1958, Phys. Rev, **112**, 1940 53

Schott. 2007, TIE-29: Refractive Index and Dispersion, Tech. rep., Schott AG 17

—. 2010, Temperature Coefficient of the Refractive Indices, Test certificate, Schott AG 17

Schwartz, R. N., & Townes, C. H. 1961, Nature, **190**, 205 66

Shaklan, S., & Roddier, F. 1988, Applied Optics, **27**, 2334 23

Stokes, L. F. 1994, IEEE Circuits and Devices Magazine, **10**, 46 40

Strelnitski, V. S., Smith, H. A., Haas, M. R., et al. 1995, Airborne Astronomy Symposium on the Galactic Ecosystem, **73**, 271 vi, 52, 66

Tan, P. K., Chan, A. H., & Kurtsiefer, C. 2016, MNRAS, **457**, 4291 50

Tan, P. K., Yeo, G. H., Poh, H. S., Chan, A. H., & Kurtsiefer, C. 2014, ApJ, **789**, L10 iv, 36, 37, 40, 63

Taylor, F. W. 1983, Nature, **306**, 640 vi, 52

Tellis, N. K., & Marcy, G. W. 2015, Publications of the Astronomical Society of the Pacific, **127**, 952 vi, 66

Thum, C., Strelnitski, V. S., Martin-Pintado, J., Matthews, H. E., & Smith, H. A. 1995, A&A, **300**, 843 52

Townes, C. H. 1983, PNAS, **80**, 1147 vi, 66

van Cittert, P. H. 1934, Physica, **1**, 201 iv, 3, 39, 63

van der Hucht, K. A. 2001, New Astronomy Reviews, **45**, 135 66

Varshni, Y. P., & Nasser, R. M. 1986, Astrophysics and Space Science, **125**, 341 52

Weaver, H., Williams, D. R., Dieter, N., & Lum, W. 1965, Nature, **208**, 29 52

Wiener, N. 1930, Acta Mathematica, **55**, 117 39

Woolf, H. M. 1968, On the computation of solar elevation angles and the determination of sunrise and sunset times, Tech. rep., NASA technical memorandum X-1646 37, 46

Zernicke, F. 1938, Physica, **5**, 785 iv, 3, 39, 63